Published in final edited form as:

Sci Transl Med. 2023 November 29; 15(724): eabo5217. doi:10.1126/scitranslmed.abo5217.

Radiation-induced bone loss in mice is ameliorated by inhibition of HIF-2α in skeletal progenitor cells

Wendi Guo[1,2], **Jiaul Hoque**[1], **Carolina J. Garcia Garcia**[3,4], **Kassandra V. Spiller**[1,5,†], **Abigail P. Leinroth**[1,6,†], **Vijitha Puviindran**[1], **Cahil K. Potnis**[1], **Kiana A. Gunn**[1,2], **Hunter Newman**[1,7], **Koji Ishikawa**[1,8], **Tara N. Fujimoto**[4], **Denae W. Neill**[9], **Abagail M. Delahoussaye**[4], **Nerissa T. Williams**[10], **David G. Kirsch**[2,10,11,†,12,†,13,†], **Matthew J. Hilton**[1,14], **Shyni Varghese**[1,7,15], **Cullen M. Taniguchi**[4,16], **Colleen Wu**[1,2,12,*]

[1]Department of Orthopaedic Surgery, Duke University School of Medicine; Durham, NC 27705, USA

[2]Department of Pharmacology & Cancer Biology, Duke University School of Medicine; Durham, NC 27705, USA

[3]UTHealth Graduate School of Biomedical Sciences, The University of Texas MD Anderson Cancer Center; Houston, TX 77030, USA

[4]Department of Experimental Radiation Oncology, The University of Texas MD Anderson Cancer Center; Houston, TX 77030, USA

[5]Department of Surgery, Duke University School of Medicine, Durham, NC 27705, USA

[6]Regeneron Pharmaceuticals, Tarrytown, NY 10591, USA

[7]Department of Mechanical Engineering and Materials Science, Duke University; Durham, NC 27705, USA

[8]Department of Orthopaedic Surgery, Showa University School of Medicine, Tokyo, 142-8666, JP

[9]Department of Radiation Physics, The University of Texas MD Anderson Cancer Center; Houston, TX 77030, USA

[10]Department of Radiation Oncology, Duke University School of Medicine; Durham, NC 27705, USA

[11]Department of Biomedical Biophysics, University of Toronto, Toronto, ON, M5S 1A8, CA

[12]Department of Radiation Oncology, University of Toronto, Toronto, ON, M5T 1O5, CA

[13]Princess Margarat Cancer Centre, University Health Network, Toronto, ON, M5G 2C1, CA

[14]Department of Cell Biology, Duke University School of Medicine; Durham, NC 27705, USA

[*]Corresponding Author: colleen.wu@duke.edu.

[†]Current address

Author contributions: WG, CW, MJH, SV, DGK, and CMT conceptualized the study. WG, JH, CJGG, CMT, and CW were involved in developing the methodology. WG, JH, CJGG, KVS, APL, CKP, KAG HN, VP, KI, TNF, DWN, AMD, NTW, and CW participated in the investigation. WG, JH, and CW performed visualization. MJH, SV, CMT, DGK, and CW provided supervision and acquisition of funding. WG, JH, and CW wrote the original manuscript and WG, JH, CJGG, TNF, DWN, AMD, NTW, MJH, DGK, SV, CMT, and CW reviewed and edited the manuscript.

[15]Department of Biomedical Engineering, Duke University School of Medicine; Durham, NC 27705, USA

[16]Department of GI Radiation Oncology, The University of Texas MD Anderson Cancer Center; Houston, TX 77030, USA

Abstract

Radiotherapy remains a common treatment modality for cancer despite skeletal complications; however, there are currently no effective treatments for radiation-induced bone loss. The consequences of radiotherapy on skeletal progenitor cell (SPC) survival and function remain unclear. Following radiation, leptin receptor-expressing cells, which include a population of SPCs, become localized to hypoxic regions of bone and stabilize the transcription factor hypoxia-inducible factor-2α (HIF-2α), thus supporting a role for HIF-2α in the skeletal response to radiation. Here, we conditionally knocked out HIF-2α in leptin receptor-expressing cells and their descendants in mice. Radiation therapy in wildtype mice reduced bone mass; however, HIF-2α conditional knockout mice maintained bone mass comparable to non-irradiated controls. HIF-2α was shown to negatively regulate the number of SPCs, the production of bone forming osteoblasts, and bone mineralization. To test whether blocking HIF-2α pharmacologically could reduce bone loss during radiation, we administered a selective HIF-2α inhibitor (PT2399), whose structural analog recently received FDA approval, to wildtype mice before radiation exposure. Pharmacological inhibition of HIF-2α was sufficient to prevent radiation-induced bone loss in a single-limb irradiation mouse model. Since approximately 90% of patients using HIF-2α inhibitor treatment develop anemia due to off-target effects, we developed a bone-targeting nanocarrier formulation to deliver the HIF-2α inhibitor to bone, in order to increase on-target efficacy and reduce off-target toxicities. Nanocarrier-loaded PT2399 prevented radiation-induced bone loss in mice while reducing drug accumulation in the kidney. Targeted inhibition of HIF-2α may therefore represent a therapeutic approach for protecting bone during radiation therapy.

INTRODUCTION

Approximately 50% of all patients with cancer receive radiotherapy over the course of their treatment (1, 2), however, skeletal complications are a commonly recognized adverse outcome in this patient population. Radiation treatment leads to increased risk of rib fractures in breast cancer patients (1.8-19% incidence) (3, 4), pelvic insufficiency fractures in patients suffering from gynecological cancers (4-45.2% incidence) (5–8), and late-onset fractures in women receiving radiotherapy for lower extremity soft-tissue sarcomas (9). As the survival rate of cancer patients continues to improve, so too does the need to prevent secondary effects of radiotherapy as it represents a substantial disease burden in patients (10). Clinical agents to treat radiation-induced bone loss in patients have not been established nor have they been translated into effective treatment regimens. As such, there is a great need to identify therapeutic targets that can ameliorate the consequences of radiotherapy.

The biological underpinnings of radiation-induced bone loss are incompletely understood. Bone-resident cells respond to extrinsic signals derived from the specialized niche of the

bone microenvironment to support normal function. Radiation induces robust changes to the bone microenvironment, including overall decreases in bone marrow cellularity, disruption of marrow vasculature, production of free radicals, and disruption of intrinsic paracrine signaling factors (11–14). This altered bone microenvironment may contribute in part to the nature of bone injury in patients undergoing radiation therapy.

The bone microenvironment is characterized by steep oxygen gradients, with oxygen tensions decreasing from the peripheral endosteal regions towards the central medullary cavity (15). This hypoxic environment is essential for maintaining homeostasis by regulating the function of resident cells including osteoprogenitors, endothelial cells, chondrocytes and hematopoietic stem cells (HSCs) (15–21). Cellular responses to hypoxia are mediated primarily through the hypoxia-inducible factor (HIF) transcription factor signaling pathway. The contribution of hypoxia and HIF signaling in regulating skeletal progenitor cell (SPC) function has not been deeply investigated.

SPC subsets in the bone marrow stroma express distinguishing markers, such as *Nestin*, leptin receptor (*Lepr*), paired-related homeobox 1 (*Prx1*), and collagen 1α1 (*Col2a1)*, enabling cell type-specific labeling or genetic modification (22–25). *Nestin*+ cells are localized to perivascular regions where oxygen tensions range from 1.3-3% O_2 (15). *Lepr*+ SPCs, the major source of osteoprogenitors in adulthood, also lie in close association with the vasculature, suggesting SPC behavior may also be intimately tied to their hypoxic niches (23). In addition, bone formation is enhanced when HIF-2α is conditionally ablated in *Prx1* or *Col1α1* expressing cells demonstrating that HIF-2α serves as a negative regulator of bone formation (26, 27). Together these data suggest that the hypoxic bone microenvironment facilitates the properties and function of SPCs and their descendants. Thus, we hypothesized that targeting the HIF-2α signaling pathway in a SPC population and their descendants may serve as an effective therapy for radiation-induced bone loss.

LepR+ SPCs contribute to new bone after radiation damage (23). Therefore, we tested our hypothesis by employing a *Lepr*-Cre model to conditionally knockout HIF-2α to study the role of HIF-2α in SPC function and their descendants upon radiation injury and subsequent recovery . In addition to genetically manipulating the HIF-2α signaling pathway, selective pharmacological inhibition of HIF-2α can be achieved through the use of clinical inhibitors such as PT2399 and structural analogues, which are being investigated in clinical trials for renal cell carcinoma (28). Systemic administration of such compounds has led to adverse events, particularly anemia, caused by the reduction of circulating EPO due to renal HIF-2α inhibition can contribute to dose-limiting toxicities (28, 29). Only recently, bone targeting drug delivery systems such as nanoparticles have been proposed to treat skeletal disorders and may offer advantages such as improved bioavailability and decreased systemic toxicity (30–32). However, these technologies are still nascent, and more research is needed to establish the efficacy of bone targeting nano-based therapeutics. Towards this end, by encapsulating PT2399 within a nanocarrier conjugated to alendronate, we generated a bone targeting delivery system to improve drug retention and release specifically at the site of mineralized bone tissue, thereby minimizing off-target effects to kidney.

This study explores the contributions of HIF-2α signaling in SPC populations and their descendants after radiation-induced microenvironment changes. HIF-2α was identified as a regulator of bone formation in the context of radiation therapy which can be targeted using the HIF-2α inhibitor, PT2399, to prevent radiation-induced bone loss. Finally, a bone-targeting nanocarrier is employed to enhance site-specific drug retention and minimize off-target toxicities.

RESULTS

Radiation exposure disrupts the perivascular niche and alters the hypoxia landscape.

To investigate the effects of radiation on bone, 12-16 week old wild-type (WT) mice were subjected to single fraction 4 Gy total body irradiation (TBI). Body weights of irradiated and non-irradiated animals were indistinguishable throughout the study, thus indicating that a modest dose of 4 Gy TBI did not induce substantial or lethal toxicity that would result in organ failure or weight loss (fig. S1, A and B). Microcomputed tomography (microCT) and hematoxylin and eosin (H&E) histological analysis at 7 and 14 days post-irradiation revealed a reduction in trabecular bone volume (Tb.BV) 14 days post-irradiation compared with non-irradiated controls (Fig. 1, A and B). Similarly, trabecular number (Tb.N) decreased with a corresponding increase in trabecular separation (Tb.Sp) starting 7 days post-irradiation with further deterioration of the aforementioned bone parameters observed 14 days post-irradiation (Fig. 1, C and D). No changes in trabecular thickness (Tb.Th) were observed at the time points investigated, suggesting that this parameter is less sensitive to radiation damage (Fig. 1E). Overall, these findings indicate that exposure to 4 Gy TBI induces trabecular bone loss in mice.

Although it is well-accepted that radiation exposure results in bone loss, the cellular mechanisms underlying this phenomenon remain unclear. LepR+ cells bone contain a population of SPC that contribute to bone repair following radiation (23).

Lepr^{cre};*Gt(ROSA)26*$^{tdTomato/+}$ (*Lepr*-tdTm) reporter mice were generated to investigate the effects of radiation on LepR+ cells and their supporting niche in the bone microenvironment. Specificity of Cre recombinase expression was confirmed by confocal analysis of spleen, kidney, liver, muscle, pancreas, and brain tissues isolated from *Lepr*-tdTm mice. Apart from the liver, no discernable tdTm+ cells noted in the tissues analyzed (fig. S1C). Following 4 Gy TBI, confocal imaging revealed dynamic changes in the bone vasculature and *Lepr*-tdTm+ reporter population (Fig. 1F, fig. S1D). Subsequent flow cytometry analysis revealed an 8-fold expansion of *Lepr*-tdTm+ cells 3 days following radiation treatment ($p \leq 0.001$) (Fig. 1, G and H, fig. S1E). This transient expansion of the *Lepr*-tdTm+ stromal cell population resolved to baseline by 14 days post-irradiation, suggesting that *Lepr*-tdTm+ cells rapidly expand in the first 3 days following radiation injury (Fig. 1, F to H). Visualization of endomucin+ vessels revealed changes in vascular morphology 3 days post-irradiation coinciding with a 5-fold increase in endomucin+ endothelial cells when assessed by flow cytometry ($p \leq 0.05$) (Fig. 1, F, I and J). However, this radiation-induced vasodilation was transient and resolved to baseline numbers by 14 days post-irradiation (Fig. 1, I and J). Confocal imaging revealed that *Lepr*-tdTm+ cells remain closely associated with the vasculature during the dynamic changes in the bone microenvironment following

radiation (Fig. 1F, fig. S1C). These findings suggest that cellular responses of LepR+ cells may be influenced by changes in the bone microenvironment caused by the disruption of the bone vasculature.

The bone vasculature serves to transport oxygen, thus damage to this network can subsequently alter homeostatic oxygen tensions present in the bone microenvironment. The effects of radiation on oxygen tension within the bone remains largely unknown. To investigate the implications of radiation on hypoxic bone niches, animals were injected with pimonidazole, a chemical probe for visualizing hypoxia, 14 days post-irradiation. Radiation resulted in robust changes to pimonidazole staining patterns. Specifically, animals receiving 4 Gy TBI had enhanced pimonidazole staining, suggesting a conversion of the homeostatic bone microenvironment to a more hypoxic niche (Fig. 1K). Moreover, in both irradiated and non-irradiated animals, *Lepr*-tdTm+ cells were found to be highly colocalized to hypoxic regions (Fig. 1, K and L). Supporting the findings in the imaging analysis, flow cytometry of cells isolated from long bones of irradiated *Lepr*-tdTm reporter mice revealed a 2-fold increase in pimonidazole+ cells compared with non-irradiated controls ($p \leq 0.001$) with the majority of *Lepr*-tdTm+ cells co-stain for pimonidazole (Fig. 1, M and N). These findings indicated that oxygen tension likely plays a key role in LepR+ cell function and prompted us to further investigate the relationship between radiation-induced changes to oxygen tension and bone repair processes facilitated by LepR+ cells.

Hypoxia and HIF-2α regulate osteoblastogenesis and mineralization of SPCs.

Hypoxia serves as an important regulator of cellular function through the activation of HIF signaling. To determine the potential impact of hypoxia on LepR+ progenitors, bone marrow stromal cells (BMSCs) were derived from *Lepr*-tdTm mice for in vitro assays. Flow cytometry analysis of BMSCs and enumeration of tdTm+ colonies confirmed that the majority of BMSCs and BMSC-derived colony-forming unit fibroblasts (CFU-Fs) (approximately 94%) were tdTm+ demonstrating that a purified population of *Lepr*-tdTm+ BMSCs can be readily attained for subsequent cultures (Fig. 2, A to D). Under hypoxic conditions (1% O_2), cultured CFU-Fs exhibited an increase in colony number, suggesting that hypoxia promotes the expansion of LepR+ progenitors *in vitro* (Fig. 2, E and F, **fig. 2SA**). To investigate the effect of hypoxia on SPC osteogenic differentiation, BMSCs were cultured under conditions of normoxia (21% O_2) and hypoxia (2% O_2). Compared with normoxia, osteogenic differentiation of BMSCs under hypoxia was impaired, as measured by a reduction in alkaline phosphatase (ALP) staining and reduced mRNA expression of osteogenic genes such as *Bsp* and *Bglap* (fig. S2A, Fig. 2, G and H). Consistent with these in vitro findings, previous studies have shown that HIF-2α negatively regulates osteoblastogenesis (26, 27). As such, subsequent studies aimed to determine if HIF-2α serves as a critical component for maintaining bone homeostasis in skeletal progenitors, particularly in the context of radiation stress response. First, in WT mice, BMSC expression of HIF-2α under 1% and 2% O_2 was explored to mimic extravascular physiological hypoxia within the bone marrow (15). Western blot analysis demonstrated that HIF-2α protein is stabilized under both 1% and 2% O_2 in BMSCs (Fig. 2I). Similarly, there was an oxygen tension-dependent induction of HIF target genes including *Glut1*, *Pgk*, and *Bnip3* (Fig. 2, J to L). To further interrogate the role of HIF-2α in BMSCs, a *Lepr*-specific HIF-2α

conditional knockout (HIF-2α cKO) mouse was generated. Polymerase chain reaction (PCR) analysis of genomic DNA from HIF-2α cKO-derived BMSCs revealed efficient Cre-mediated recombination as confirmed by the presence of the recombined 1-loxP allele (fig. S2B). Moreover, both a concordant decrease in the expression of the mRNA encoding HIF-2α (*Epas1*) (fig. S2C) and HIF-2α protein were observed in whole bone homogenates of HIF-2α cKO mice and BMSC derived from control versus HIF-2α cKO animals (Fig. 2M). BMSCs isolated from HIF-2α cKO also showed a modest increase in pro-osteogenic *Bglap* and *Bsp* mRNA expression (Fig. 2, N and O). In vivo, *Epas1* mRNA expression was upregulated in response to radiation-induced stress in WT cells (Fig. 2P). Collectively, these findings indicate that HIF-2α signaling has important implications in the LepR+ SPC population, particularly in the context of radiation injury.

Loss of HIF-2α alters the transcriptomic profile within LepR+ cells.

To begin to interrogate transcriptomic differences resulting from the conditional ablation of HIF-2α in LepR+ cells and their descendants after radiation exposure, bulk RNA sequencing was performed on *Lepr*-tdTm+ cells isolated 14 days post-irradiation from *Lepr*-tdTm WT control and mice with both *Lepr*-tdTm and *Lepr*-specific HIF-2α cKO reporter animals (*Lepr*-tdTm-HIF-2α cKO). Analysis revealed 840 differentially expressed genes (DEG) (p-value of 0.05). Of these genes, 496 were upregulated and 344 were downregulated (fig. S3A). A portion of DEG (>1.5-fold difference in gene expression) were clustered and depicted as a heatmap (Fig. 3A). As expected, a decrease in *Epas1*, which encodes for HIF-2α, was noted in *Lepr*-tdTm+ cells of the cKO mouse, validating the murine model (Fig. 3A). Genes associated with the heat shock response were some of the most highly downregulated genes in the absence of HIF-2α (*Hsph1, Hspa8, Dnaja1, Hsp90b1, Hspa5, Hspa1a, Dnajb9*). An upregulation of genes associated with bone mineralization (*Bglap, Bglap2*), cell cycle (*Cdk5rap1*), and metabolic function (*Slc22a4, Slc2a4*) was also observed in irradiated HIF-2α cKO derived cells (Fig. 3A). Functional gene ontology (GO) enrichment analysis revealed downregulation of biological processes related to protein folding and upregulation of biological processes related to metabolic function, erythrocyte development, and homeostasis with conditional HIF-2α loss (Fig. 3, B and C). These changes were not noted between irradiated and non-irradiated HIF-2α cKO samples, demonstrating irradiation alone did not account for observed changes (fig. S3, B and C). Increases in DNA damage and repair pathways were observed between *Lepr*-tdTm+ cells from non-irradiated and irradiated *Lepr*-tdTm reporter mice indicating that the 4 Gy TBI dose of irradiation likely induced DNA damage (fig. S3D). Collectively, our transcriptomic analysis suggests that following radiation HIF-2α positively regulates stress/protein folding and negatively regulates cell cycle, osteogenic, and metabolic function in LepR+ cells and their descendants in the bone microenvironment.

HIF-2α cKO prevents loss of LepR+ cells and maintains homeostatic bone microenvironmental hypoxia.

To expand upon and validate the transcriptomic analysis, we sought to determine the cellular effects of HIF-2α loss on the *Lepr*-tdTm+ SPC population. The total number of *Lepr*-tdTm+ cells during the initial expansion period 3 days post-irradiation was unchanged between *Lepr*-tdTm (control) and *Lepr*-tdTm-HIF-2α cKO mice (fig S4, A and B). The number

of *Lepr*-tdTm+ cells remaining 14 days post-irradiation was increased by approximately 2.5-fold in irradiated *Lepr*-tdTm-HIF-2α cKO mice animals compared with *Lepr*-tdtm control ($p \leq 0.001$) (Fig. 3, D and E). 14 days post-irradiation, bone marrow isolates were extracted from irradiated *Epas1*$^{fl/fl}$ littermate control or HIF-2α cKO mice for progenitor cell analysis by CFU-F assays. As expected, cells derived from WT bone marrow, fewer CFU-Fs were produced from 4 Gy irradiated mice compared with 0 Gy TBI (fig. S4, C and D). Minimal mineralization was also observed in irradiated vs non irradiated cells WT BMSCs, as assessed by alizarin red (AR) staining after CFU-Fs were treated with osteogenic media (fig. S4, C and E). In contrast, consistent with the increased numbers of tdTm+ cells seen in *Lepr*-tdTm-HIF-2α cKO mice 14 days post-irradiation when compared to tdTm-*Epas1*$^{fl/fl}$ littermate control mice (Fig. 3, D and E), HIF-2α cKO bone marrow had a 9-fold increase in the number of CFU-Fs compared with 4 Gy irradiated *Epas1*$^{fl/fl}$ littermate control (Fig. 3, F and G). To test if ablation of HIF-2α affects SPC osteogenic differentiation, CFU-Fs were treated with osteogenic media and cultured for an additional 14 days to evaluate functional mineralization AR staining (Fig. 3F). Indeed, HIF-2α cKO animals demonstrated a 10-fold increase in mineralization compared with controls which had close to zero mineralized colonies following radiation (Fig. 3, F to H). These data suggest that HIF-2α negatively regulates the number of *Lepr*-tdTm+ progenitors and their osteogenic lineage specification following radiation injury.

Immunofluorescent images demonstrated that radiation markedly increased pimonidazole staining for hypoxia in the bone microenvironment as early as 3 days post-irradiation and persisted up to 14 days post-irradiation (Fig. 3, I and J). There was reduced hypoxia staining (pimonidazole) in *Lepr*-tdTm-HIF-2α cKO mice at both 3 and 14 days post-irradiation, suggesting that loss of HIF-2α in *Lepr*-tdTm+ progenitors protects against radiation-induced changes in oxygen tension within the bone microenvironment (Fig. 3, I and J, fig. S4F). A closer look into the hypoxic landscape revealed profound differences between irradiated control and *Lepr*-tdTm-HIF-2α cKO animals. Following irradiation, control animals had substantial pimonidazole staining throughout the marrow cavity and to a lesser extent along trabecular bone surfaces (fig. S4F, Fig. 3I). In contrast, bone marrow of irradiated *Lepr*-tdTm-HIF-2α cKO animals was characterized by robust pimonidazole staining along bony surfaces with substantial colocalization of *Lepr*-tdTm+ cells, with less pimonidazole staining being observed throughout the marrow cavity (Fig. 3, I and J, fig. S4F). Collectively, these data indicate that radiation transforms the hypoxic bone landscape, however, deletion of HIF-2α in the LepR+ population may create a more radioresistant bone microenvironment possibly through altered metabolic function.

HIF-2α cKO in LepR+ cells prevents radiation-induced bone loss.

Based on in vitro and in vivo observations that HIF-2α signaling mediates biological responses to radiation exposure in LepR+ cells and their descendants, 12–16 week old WT control and HIF-2α cKO mice were further analyzed. Next, 12-16 week old control (*Epas1*$^{fl/fl}$) and HIF-2α cKO mice were exposed to 4 Gy TBI to evaluate bone parameters by microCT. As expected, histological examination and microCT analyses revealed that 4 Gy TBI reduced Tb.BV/TV in irradiated control animals compared with non-irradiated counterparts (Fig. 4, A to C). In contrast, microCT quantification of bone parameters

revealed that irradiated HIF-2α cKO have increased Tb.BV/TV, Tb.N, and decreased Tb.Sp when compared with irradiated control mice (Fig. 4, C to E). Although no differences in Tb.Th were observed between non-irradiated and irradiated control mice, irradiated HIF-2α cKO increased Tb.Th when compared with irradiated controls (Fig. 4F). MicroCT analysis of non-irradiated 14 week old WT mice revealed no differences in reported bone parameters between 0 and 14 days, thus demonstrating that the observed changes in bone phenotypes were not attributed to baseline bone formation over the measured time period (fig. S5, A to D). No differences were observed in cortical parameters including cortical area per total tissue area (Ct.A/TA) and cortical thickness (Ct.Th) between non-irradiated and irradiated control mice. Nevertheless, HIF-2α cKO animals exhibited increased Ct.A/TA and Ct.Th compared with both non-irradiated and irradiated controls (Fig. 4, A, G and H).

Stabilization and activation of HIF-1α also occurs under hypoxic conditions with HIF-1α and HIF-2α having both distinct and overlapping functions (33). Therefore, to test HIF isoform specificity of our bone phenotype, *Lepr*-specific HIF-1α cKO (HIF-1α cKO) mice were generated and subjected to 4 Gy TBI. Western blot analysis of BMSCs cultured at 1% O_2 revealed hypoxic induction of HIF-1α in BMSCs isolated from control Cre negative (*Hif1a*$^{fl/fl}$) mice, but not from HIF-1α cKO mice thus confirming efficient Cre-mediated recombination in HIF-1α cKO animals (fig. S5E). Unlike HIF-2α cKO mice, microCT analysis revealed that conditional loss of HIF-1α in *Lepr*-expressing cells and their decendants did not mitigate bone loss after radiation exposure (Fig. 4, I to M). In addition, under homeostatic conditions, long bones derived from HIF-2α cKOs animals appeared overtly normal, and microCT analyses failed to identify any differences in bone parameters between knockout and control mice (fig. S5, F to J). Collectively, these findings indicate that conditional ablation of HIF-2α, but not HIF-1α, in the context of radiation exposure provides protection and in some cases enhances bone accumulation.

To begin to understand the downstream effects of loss of HIF-2α in the LepR+ population, static and dynamic histomorphometry was used to assess osteoclast and osteoblast activity following radiation treatment in control and HIF-2α cKO animals. Conditional loss of HIF-2α did not affect bone resorption as no changes were observed in tartrate-resistant acid phosphatase (TRAP) stained osteoclast number per bone surface (Oc.N/BS) nor active resorption sites evidenced by the extent TRAP-labeled surface relative to bone surface (Oc.S/BS) (Fig. 4, N to P). Although no differences were found in osteoblast number/bone surface between irradiated control and knockout mice (fig. S5K), evaluation of osteoblastic bone formation through calcein and alizarin red double labeling confirmed that HIF-2α cKO animals had increased osteoblast coverage as demonstrated by increased mineralized surface per total bone surface (MS/BS) (Fig. 4, Q and R). Similarly, mineral apposition rate (MAR) and bone formation rate (BFR) were increased in HIF-2α cKO relative to controls (Fig. 4, S and T). Diminished bone volume during aging and in certain obesity models is often associated with a concomitant increase in marrow adiposity, due in part, to skewed lineage potential of skeletal progenitors (34). As such, we assessed marrow adiposity by performing osmium tetroxide staining and microCT analysis on long bones isolated from irradiated control and HIF-2α cKO mice. As expected, there was an increase in adipocyte volume/total volume (AV/TV) in Cre negative (*Epas1*$^{fl/fl}$) control irradiated mice when compared with non-irradiated controls; however, no changes were noted in marrow adipose tissue between

control and HIF-2α cKO mice after radiation exposure (Fig. 4U). Overall, these findings suggest that HIF-2α is not a major contributor to osteoclast activity, nor aberrant adipocyte lineage commitment in the context of 4 Gy TBI, but rather HIF-2α contributes to the mineralization and bone-forming activities of osteoblasts in HIF-2α cKO animals which may partially account for the increase in bone volume seen in HIF-2α cKO animals.

Pharmacological inhibition of HIF-2α ameliorates radiation-induced bone loss.

Currently available HIF-2α inhibitors such as PT2399, target the HIF-2α Per-ARNT-Sim (PAS)-B domain, thereby preventing the formation of the heterodimer complex necessary for downstream activity (Fig. 5A) (35). PT2399 and similar analogues are actively used in clinical trials for renal cell carcinoma and recurrent glioblastoma demonstrating favorable safety profiles (28, 29). As such, PT2399 serves as a promising tool to interrogate the effect of HIF-2α inhibition on bone following radiation treatment with high clinical translatability. Administration of PT2399 was hypothesized to offer therapeutic benefits to radiation-injured bone. In cultured BMSCs, PT2399 inhibited the expression of HIF-2α protein (Fig. 5B, fig. S6A). A focal radiation model, similar to the delivery of image-guided radiation therapy, was established at a dose of 8 Gy (anterior-posterior/posterior-anterior) AP/PA, applied to the right hindlimb (Fig. 5C, fig. S6B). Shortly following the first dose, 12 week old WT C57/B6 mice were administered 50 mg/kg of PT2399 or vehicle twice daily by oral gavage with the exception of two washout periods at days 5, 6, and 12-14 (Fig. 5D). The effects of PT2399-mediated HIF-2α inhibition on bone parameters were evaluated 14 days post-radiation. Similar to the genetic HIF-2α cKO model, 3D microCT reconstruction imaging revealed that PT2399 treatment in the absence of radiation does not change bone volume (Fig. 5E). However, in the presence of radiation, microCT and H&E histological analysis revealed treatment with PT2399 ameliorated radiation-induced bone loss (Fig. 5, E to G).

Mice treated with PT2399 were grossly normal with no signs of morbidity across all treatment conditions. All treatment groups exhibited similar overall percent body weight across all measured time points indicating that a modest dose of focal 8 Gy radiation and PT2399 treatment do not induce excessive systemic toxicities (Fig. 5H). However, as reported in previous studies, twice daily oral administration of PT2399 resulted in reduced red blood cell (RBC) counts and hemoglobin (HGB) amounts compared with vehicle treated animals (Fig. 5, I and J). Kidney homogenates had reduced *Epo* mRNA transcripts with oral PT2399 treatment following 8 Gy local radiation (Fig. 5K). In response to diminished RBC counts and HBG concentration, an increase in serum EPO concentration is often observed. Functionally, this is a compensation mechanism to increase erythropoiesis, elevate RBCs, and overcome anemia. Mice treated with PT2399 following focal irradiation had elevated serum EPO concentration compared with irradiated vehicle control (Fig. 5L). Collectively, these data highlight that although PT2399 can potentially serve as a powerful clinical therapeutic to prevent radiation-induced bone loss, there is a need for alternative treatment strategies that can produce the desirable effects of bone radioprotection while minimizing off-target kidney toxicities.

HIF-2α nanocarriers enable bone-targeting.

To enhance bone-targeting of the therapeutic and minimize systemic impact on homeostatic renal EPO production, a targeted nanocarrier approach was developed. To confer bone-binding affinity, alendronate (Aln), a second-generation bisphosphonate, was conjugated to methacrylated hyaluronic acid (HA-MA) to form HA-MA-Aln (Fig. 6A, fig. S7). Nanocarriers (NC) were generated by copolymerizing HA-MA-Aln, poly(ethylene glycol) diacrylate (PEGDA), and methacrylated-PT2399 by an inverse emulsion suspension polymerization method (fig. S7) to produce NCs that localize to sites of mineralized tissue (Aln-PT-NC) (Fig. 6A). A control nanocarrier devoid of bone-targeting Aln was synthesized similarly using HA-MA and methacrylated-PT2399 (Ctrl-PT-NC). Nanocarriers were characterized using a combination of FTIR, ^{1}HNMR spectroscopy, and UV–Visible spectrophotometry to confirm successful synthesis and incorporation of PT2399 without structural changes (fig. S8 to S11).

To test bone-binding affinity of Aln nanocarriers, HA-MA and HA-MA-Aln were conjugated with cyanine 7 (Cy7) fluorophore through amide coupling to produce fluorescently tagged, Ctrl-PT-NC and Aln-PT-NC (fig. S8). For in vivo biodistribution analyses, 12 week old animals received a single tail vein injection of either Ctrl-PT-NC or Aln-PT-NC, and subsequent visualization of fluorescently tagged nanocarrier was carried out with an in vivo imaging system (IVIS) (30). After 4 days, fluorescent signal was highly localized at mineralized tissue sites in Aln-PT-NC treated animals, particularly the ribcage and spinal column (Fig. 6B). Furthermore, broad signal was visualized in the forelimbs and hindlimbs of animals receiving Aln-PT-NC, however, no such signal was present in Ctrl-PT-NC treated animals (Fig. 6B). Fluorescence signal from both nanocarriers was still detectable 20 days post-injection (Fig. 6C). Similar to early time points, ventral view images showed robust signal from forelimbs and hindlimbs in animals treated with Aln-PT-NC compared with nanocarriers without Aln moieties, suggesting that Aln nanocarriers stay bound to bone tissue long-term (Fig. 6C). Collectively, these findings demonstrate that Aln-PT-NCs can rapidly bind bone tissue and remain detectable in tissues for at least 20 days.

Further evaluation of nanocarrier biodistribution 48 hours post-injection was performed by post-mortem analysis of tissue. For Ctrl-PT-NCs, fluorescence intensity was highest in the kidney followed by the liver and spleen (fig. S12, A and B). Conversely, for Aln-PT-NCs, signal accumulation was highest in the liver followed by spleen and vertebrae (fig. S12, C and D). Aln-PT-NC nanocarrier accumulation was increased 2-3-fold in the lumbar vertebrae (Fig. 6, D and E), femurs (Fig. 6, F and G), and tibiae (Fig. 6, H and I) of treated animals compared with Ctrl-PT-NC treatment ($p < 0.01$). Aln-PT-NC treated animals demonstrated a nearly 4-fold decrease ($p < 0.001$) in fluorescence intensity in the kidney compared with animals treated with Ctrl-PT-NC, suggesting a substantial decrease in off-target renal drug accumulation (Fig. 6, J and K). Instead, Aln-PT-NC treatment led to higher fluorescence signal in the liver, suggesting that Aln-PT-NC clearance favors hepatic metabolism compared with Ctrl-PT-NC which appeared biased towards renal clearance (Fig. 6, J and K, fig. S12, E and F). Animals treated with Aln-PT-NC also had increased spleen fluorescence compared with Ctrl-PT-NC (fig. S12, G and H). Minimal nanocarrier

accumulation was observed in the lung (fig. S12, I and J), heart (fig. S12, K and L), brain (fig. S12, M and N), and muscle (fig. S12, O and P) in both treatment groups, although Ctrl-PT-NCs were modestly increased in the brain over Aln-PT-NCs. Taken together, these findings implicate Aln-PT-NC as a potential therapeutic with favorable pharmacokinetic properties that potentially reduces tissue toxicity to the kidney.

Aln-PT-NC rescues radiation-induced bone loss.

To investigate the therapeutic efficacy of bone-targeted inhibition of HIF-2α with Aln-PT-NCs, 12 week old mice were irradiated with a single fraction of 4 Gy TBI and dosed systemically, intravenously by tail vain injections twice weekly intervals with Aln-PT-NC at a PT2399 dosage of 50 mg/kg (Fig. 7A). Control animals were treated with similar mg/kg body weight of Aln nanocarrier devoid of PT2399 (Aln-NC) (Fig. 7A). No differences in weight were observed between non-irradiated, irradiated Aln-NC, and irradiated Aln-PT-NC animals by 14 days post-irradiation (Fig. 7B).

After 14 days, microCT and H&E analyses showed that the irradiated Aln-NC treated group had a reduction in Tb.BV/TV, Tb.N, Tb.Th, and increased Tb.Sp compared with the non-irradiated vehicle controls (0 Gy) (Fig. 7, C to G). Irradiated Aln-PT-NC treated animals were protected from trabecular bone loss as demonstrated by a nearly 2-fold increase ($p \leq 0.01$) in Tb.BV/TV ratio, increased Tb.N, Tb.Th, and decreased Tb.Sp compared with Aln-NC treated animals (Fig. 7, C to G). Aln-PT-NC treatment produced bone parameters comparable to those of non-irradiated animals (Fig. 7, D to G). Quantification of TRAP+ cells revealed no differences between osteoclast number/bone surface nor osteoclast surface/bone surface, thus confirming increases in bone parameters measured between Aln-NC and Aln-PT-NC treated mice were unlikely due to differences in osteoclast activity (Fig. 7, H and I). New bone formation was assessed by double fluorescent labeling of mineral deposition using calcein and alizarin red which were systemically administered over a 7-day interval (Fig. 7J). Histomorphometric analyses revealed increased MS/BS, MAR, and BFR in Aln-PT-NC treated animals compared with Aln-NC, suggesting that drug treatment stimulates downstream osteoblast activity similar to findings in HIF-2α cKO genetic model (Fig. 7, J to M). Importantly, Aln was dosed at a concentration of 1.8-2.2 mg/kg, twenty-five times below the therapeutic dose used in murine models of osteoporosis (36, 37). Together, these results demonstrate that Aln-PT-NC treatment has specific and strong radioprotective effects in a preclinical mouse model of radiotherapy by enhancing bone formation, thereby suggesting that administration of Aln-PT-NC could serve as a potential therapeutic strategy to treat radiation-induced bone loss.

We further examined whether administration of Aln-PT-NC minimizes off-target effects to the kidney that may decrease the development of anemia. In contrast to oral administration of PT2399, administration of Aln-PT-NC did not decrease RBC and HBG amounts when compared with Aln-NC treated animals (Fig. 7, N and O). There was no difference in kidney *Epo* mRNA transcripts or serum EPO concentration with bone-targeted Aln-PT-NC compared with unloaded Aln-NC treatment (Fig. 7, P and Q). These findings suggest that at the time points and dose tested, administration of Aln-PT-NC prevents radiation-induced

bone loss but does not lead to off-target kidney toxicity indicative of anemia that was observed in non-targeted therapy.

DISCUSSION

In the present study, we characterized the effect of radiation on the hypoxic bone microenvironment and identified a critical role for HIF-2α signaling in mediating radiation-induced bone loss. These data are reveal the following insights: 1) hypoxia in the bone microenvironment changes in response to radiation injury, 2) HIF-2α signaling in *Lepr*-expressing skeletal progenitors and their descendants is a negative regulator of bone mass in the context of radiation, and 3) a bone-targeting HIF-2α inhibitor-loaded nanocarrier alleviates radiation-induced bone loss in a preclinical murine model.

In vivo characterization of the hypoxic bone microenvironment revealed that radiation induces increased hypoxia which may be attributed to either, 1) impaired oxygen delivery due to a compromised vascular network, or 2) an increase in oxygen consumption in the cellular constituents of the bone microenvironment or both. Supporting these concepts, after radiation exposure, VEGF-mediated angiogenesis is required for recovery of the bone microenvironment and to replenish the hematopoietic compartment, robust energy demands are necessary for the differentiation of HSCs and the proliferation of their downstream progenitors (14). Although confocal and flow cytometry analysis of endomucin stained cells in the bone microenvironment 14 days post-irradiation demonstrate that both the number and structure of endomucin$^+$ vessels are comparable to non-irradiated controls; these assays did not assess the functionality of the vasculature, suggesting impaired oxygen delivery may still occur in this context. RNA sequencing studies on *Lepr*-tdTm+ cells isolated from irradiated versus non-irradiated mice suggest pathways associated with metabolic function are dysregulated in this cell population; however, altered cellular energetics within the hematopoietic compartment also likely contribute to increased oxygen consumption. Increases in hypoxia within the medullary cavity after radiation exposure coincided with increases in *Epas1* mRNA transcripts. Highlighting the importance of these observations, genetic ablation of HIF-2α in *Lepr*-expressing cells prevented bone loss after radiation exposure. On a cellular level, radiation-dependent HIF-2α-mediated bone loss in *Lepr*-tdTm-labeled cells can be attributed to multiple factors: (1) a reduction in the overall number of *Lepr*-tdTm+ SPC, (2) a decrease in the mineralization potential of skeletal progenitors, or (3) a decrease in downstream osteoblast activity following radiation injury. Collectively, these data provide evidence loss of HIF-2α, mediates bone formation in a skeletal progenitor population and their progeny following radiation injury with functional consequences for bone health. Elucidating the cellular and molecular mechanisms that contribute to the enhanced hypoxic landscape observed after radiation exposure as well as the direct and indirect role that HIF-2α signaling in *Lepr*-expressing cells plays in maintaining hypoxic homeostasis are exciting areas of future investigation.

We found that loss of HIF-2α induced bone formation in the presence of radiation but did not affect bone mass at homeostatic conditions. This finding is contrasted by recent studies using *Prx1-Cre* and *Col1α1-Cre* mouse models whereby loss of HIF-2α in *Prx1*-expressing and *Col1α1*–expressing populations resulted in increased bone mass independent of an

external stressor (26, 27). These discordant results are likely due to differences in the genetic models utilized. *Col1a1* is primary expressed by osteoblastic cells, indicating that HIF-2α signaling differentially mediates the function of the *Lepr*-expressing progenitor population from that of *Col1a1+* osteoblasts (38). In contrast, *Prx1* is more broadly expressed by early mesenchymal progenitors and their descendants with expression present in limb buds as early as 10.5 days post-conception (39). Loss of HIF-2α in early mesenchymal progenitors and their descendants results in developmental effects with *Prx1*-HIF-2α cKO demonstrating a transient delay of endochondral ossification, and overexpression of HIF-2α resulted in shorter limbs (18, 27). In contrast, the present study employs the *Lepr*-Cre model which marks a population of skeletal progenitors that appear perinatally and minimally contribute to bone prior to 2 months of age (23, 40). Thus, using this model, we can better delineate developmental phenotypes from that of postnatal, homeostatic phenotypes that contribute to adult osteogenesis. Indeed, skeletal progenitor populations, including *Lepr*-tdTm+ cells, are largely quiescent at homeostasis but mobilize in response to injury (41–43). These findings suggest a model in which radiation injury leads to the mobilization of *Lepr*-tdTm+ skeletal progenitors whose functions are critically influenced by HIF-2α signaling to mediate repair processes.

Systemic administration of PT-2399 elevated serum EPO concentrations in irradiated mice relative to mice treated with vehicle control. Several studies have demonstrated that EPO can regulate both osteoclast and osteoblast activity (44, 45). Hence, it is possible that increases in systemic EPO amounts may account, in part, for the enhanced bone formation observed after systemic administration of PT-2399. Importantly, no differences in the concentration of serum EPO were detected in mice treated with bone-targeted PT-2399, Aln-PT-NC, suggesting that alleviation of bone loss after radiation exposure is not solely dependent on the elevation of systemic EPO concentration.

The conditional genetic knockout models used here have limitations that must be considered. Recent single-cell transcriptomic analyses revealed that *Lepr*-expressing cells within the bone are highly heterogenous (46, 47). *Lepr*-tdTm+ cells consisted not only of perivascular and stromal progenitors, but also osteoblasts and adipocytes. Thus, we cannot fully delineate the contribution between the skeletal progenitor population and that of their descendants. Importantly, cell types may be differentially affected by radiation as the stage of differentiation has been shown to confer differences in radiosensitivity and the subsequent cellular responses to radiation therapy (48). Thus, the radiation response of skeletal progenitors may differ from the response of mature osteoblasts and adipocytes descendants. Likewise, skeletal progenitors and lineage descendants play an integral role in the maintenance of bone homeostasis through the secretion of bone niche supporting factors including SCF and CXCL12, thus HIF-2α loss may also impact such systemic mechanisms to play a role in pathology of radiation-induced bone loss (47). Nevertheless, this study identifies a role of HIF-2α signaling in the regulation of LepR+ skeletal progenitor number and downstream osteoblast function.

Belzutifan, a structural analogue to PT2399, was the first HIF-2α inhibitor to receive FDA approval in 2021, thereby bolstering the clinical translatability of this class of compounds (28). However, one key limitation of HIF-2α inhibitor treatment is the development of

chronic side effects in patients with approximately 90% of patients developing anemia due to the loss of HIF-2α activation of renal EPO production (28). To address this limitation, we employed a unique nanocarrier delivery system to target drug payload at mineralized tissue sites. Aln-NCs potentially resolve issues of kidney toxicity and systemic delivery of Aln-PT-NCs resulted in therapeutic efficacy. In addition, nanocarrier-based delivery may confer additional advantages including increased drug stability, specificity, favorable release kinetics and reduced side effects compared with conventional drug delivery methods (49). These results support the continued development of HIF-2α inhibitors, particularly in formulations that will allow for reduced off-target toxicity, to protect against radiation-induced bone loss.

In summary, HIF-2α signaling negatively regulates bone formation in the LepR+ SPC population following radiation injury. This study expands our limited understanding and emphasizes the multifactorial nature of radiation-induced bone loss on bone microenvironment radiosensitivity and the resulting effects on skeletal lineage cells and their descendants. Currently, there are no clinically established treatments for radiation-induced bone loss. Furthermore, bone loss, osteoporosis development, and resulting insufficiency fractures may not present until years following radiation treatment, thereby emphasizing the need for both acute and long-term treatment (50). The data presented in this study support further development and characterization of selective nanocarriers to target HIF-2α to prevent adverse bone outcomes associated with radiotherapy.

MATERIALS AND METHODS

Study design

This study was designed to test the hypothesis that HIF-2α is a potential therapeutic target for radiation-induced bone loss and to assess the therapeutic benefit of HIF-2α inhibition using a pharmacological inhibitor and bone-targeted nanocarrier technology. This hypothesis was addressed through the following methods: 1) characterizing the hypoxic bone landscape following radiation, 2) examining bone phenotypes of HIF-2α cKO mice, 3) determining the efficacy of pharmacological HIF-2α inhibition, and 4) fabricating and testing efficacy of Aln-PT-NCs in ameliorating radiation-induced bone loss. Drug studies were carried out using the HIF-2α inhibitor, PT2399. Age-matched animals were randomly assigned to different treatment groups and received the same drug dose or equivalent vehicle. A single outlier was excluded from the 8 Gy vehicle-treated group as this animal failed to respond to radiation treatment exhibiting the highest bone mass amongst all animals tested including non-irradiated animals (approximately 1.7-fold greater bone mass compared with average of 8 animals within experimental group and approximately 1.3-fold greater bone mass compared with average of 10 animals in non-irradiated, no treatment group). Pilot studies were conducted to identify appropriate endpoints by which all subsequent experimental endpoints were prospectively defined. All datasets include at least three biological replicates and three technical replicates as appropriate, with the exception of Western blot analysis ($n = 2$). Sample numbers (n) used in each experiment are indicated in the respective figure legends. Sample size was based on prior and early observation of experimental standard deviations of sample means, such that more animals were included in groups

that were observed to have greater variation in baseline values. Investigators were not blinded to sample allocation, data acquisition, or data analysis (with the exception of image quantification). Mice were housed in cages of 5 and cages were randomly assigned to either control (non-irradiated or vehicle control for pharmacological studies) or treatment (irradiated or drug for pharmacological studies) groups.

Mouse lines

All experimental procedures were approved by the Institutional Animal Care and Use Committee at Duke University (A139-22-07). Mice were group-housed in animal care facilities under a 12hr:12hr light:dark cycle at 23±2°C with water and standard diet (LabDiet #5053) ad libitum. Mice were euthanized by CO_2 asphyxiation. Experiments were performed on 12 to 16 week old male and female mice with a C57Bl/6J background. C57Bl/6J (JAX:000664), *Gt(ROSA)26*$^{tdTomato/+}$ (JAX:007909), *Lepr*^{Cre} (JAX:008320), *Epas1*$^{fl/fl}$(JAX:008407), *Hif-1a*$^{fl/fl}$ (JAX:007561), mouse strains were obtained from The Jackson Laboratory. To generate *Lepr*-tdTm mice for lineage tracking, *Lepr*^{Cre} mice were crossed with *Gt(ROSA)26*$^{tdTomato/tdTomato}$ mice. HIF-2α cKO were generated by crossing *Lepr*^{Cre} with *Epas1*$^{fl/fl}$ *to make Lepr*^{cre}*;Epas1*$^{fl/+}$ mice. These were then crossed to *Epas1*$^{fl/fl}$ mice to generate *Lepr* ^{WT}*;Epas1*$^{fl/fl}$ (control/Cre negative) or *Lepr*^{cre}*;Epas1*$^{fl/fl}$ (HIF-2α cKO) mice. The same strategy was used to generate HIF-1α cKO with *Lepr*^{Cre} and *Hif1a*$^{fl/fl}$ mice. *Lepr*-tdTm-HIF-2α cKO (cKO expressing tdTm under *Lepr*) were created by crossing *Lepr*^{cre}*;Epas1*$^{fl/fl}$ mice with *Gt(ROSA)26*$^{tdTomato/tdTomato}$ mice. *Lepr*^{cre}*;tdTm;Epas1*$^{fl/+}$ mice were then crossed to *Epas1*$^{fl/fl}$ mice to generate *Lepr*^{cre}*;tdTm;Epas1*$^{fl/fl}$ mice (*Lepr*-tdTm-HIF-2α cKO). Genotyping was performed as previously described for *Cre*, *Epas1*$^{fl/fl}$*, and Hif-1a*$^{fl/fl}$ (51).

Radiation treatment

TBI was performed using an X-RAD 320 biological irradiator (Precision X-ray Inc.) with a 2.5 mm aluminum, 0.1 mm copper filter and a field of view of 20 cm x 20 cm at a dose of 4 Gy. Dosimetry was measured with an ion chamber by the Duke University Radiation Safety Division. For TBI, unanesthetized mice were placed in a ventilated cast acrylic pie cage (Braintree Scientific) without restraints or shielding. The pie cage was centered on an acyclic slab to provide sufficient back scatter. All mice were placed 50 cm from the source and irradiated with 320 kVp, 12.5 mA X-rays. Single-limb irradiation was delivered using a small animal irradiator, X-RAD 225Cx (Precision X-Ray Inc.) or Small Animal Radiation Research Platform (SARRP, Xstrahl). Prior to treatment, animals were anesthetized with nebulized isoflurane/O_2 and positioned prone on the treatment stage. The irradiated limb received a single fraction of 8 Gy delivered anterior-posterior/posterior-anterior (AP/PA) using a motorized collimator creating a 40 mm x 30-40 mm field at the treatment isocenter covering the entire right hindlimb, including the femur, tibia, and foot.

In vivo PT2399 treatment

PT2399 (MedChemExpress, HY-108697) was prepared with 10% ethanol, 30% PEG400, 60% water containing 0.5% methylcellulose and 0.5% Tween 80 (aqueous). Mice were treated with 50 mg/kg of PT2399 or vehicle following radiation treatment twice daily by oral gavage 8-10 hours apart for 5 consecutive days followed by a 2 day wash out

period over the course of 14 days. Mice received a total of 20 doses over 14 days. Body weights were generally taken daily and treatment doses were adjusted weekly. Animals were euthanized and tissues were harvested at 14-days post-irradiation. For nanocarrier treatment, nanocarriers were suspended in sterile saline (0.9% NaCl) and administered to mice by tail vein injection at a PT2399 dosage of 50 mg/kg. The first dose was given 3 days prior to irradiation and subsequent doses were given 3-4 days apart for a total of 5 doses. For untreated animals, a similar dosage of nanocarrier devoid of PT2399 was given. Animals were euthanized and tissues were harvested at 14-days post-irradiation.

Statistical analysis

Statistical analysis was performed using GraphPad Prism 9, version 9.2.0. All reported *p*-values were obtained from 1) unpaired, two-tailed tests (when comparing two groups) with a confidence level of 95%, and a *p*-value < 0.05 considered to be statistically significant, or 2) analysis of variance (ANOVA) testing followed by Tukey's post hoc (when comparing more than two groups) at the 0.05 significance level. Shapiro-Wilk test was used to test for normality of data. Statistical tests for each experiment are indicated in figure legends, Data are presented as means ± SEM. *$p < 0.05$, **$p < 0.01$, ***$p < 0.001$, and ****$p < 0.0001$. All experiments were performed on ≥3 individual biological samples, sample numbers are provided in figure legends.

Supplementary Material

Refer to Web version on PubMed Central for supplementary material.

Funding:

This work was supported by National Institute of Arthritis and Musculoskeletal and Skin Diseases grants R01AR081303 (to CW), R01AR071552 (to SV), AR071722 (to MJH), AR076180 (to APL), the National Cancer Institute grant R35CA197616 (DGK), and National Institutes of Health grant R01CA227517-01A1 (to CMT).

Competing interests:

DGK owns stock and is on the scientific advisory board of Lumicell, which is commercializing intraoperative imaging technology. DGK is a co-founder of Xrad Therapeutics, which is developing radiosensitizers. These interests do not represent a conflict of interest with respect to the design, execution, or interpretation of the studies presented in this manuscript. The DGK laboratory receives research funding from Merck, Bristol Myers Squibb, and Varian Medical Systems, but this funding did not support the research described in this manuscript. CMT is a paid consultant for Xerient Pharmaceuticals. The remaining authors declare that they have no competing interests.

Data and materials availability:

All data associated with this study are in the paper or the supplementary materials with the exception of the raw RNA sequencing data, which has been deposited in NCBI GEO database (accession number: GSE235292).

References

1. Barton MB, Jacob S, Shafiq J, Wong K, Thompson SR, Hanna TP, Delaney GP, Estimating the demand for radiotherapy from the evidence: a review of changes from 2003 to 2012. Radiother Oncol 112, 140–144 (2014). [PubMed: 24833561]

2. Delaney G, Jacob S, Featherstone C, Barton M, The role of radiotherapy in cancer treatment: estimating optimal utilization from a review of evidence-based clinical guidelines. Cancer 104, 1129–1137 (2005). [PubMed: 16080176]

3. Overgaard M, Spontaneous radiation-induced rib fractures in breast cancer patients treated with postmastectomy irradiation. A clinical radiobiological analysis of the influence of fraction size and dose-response relationships on late bone damage. Acta Oncol 27, 117–122 (1988). [PubMed: 3390342]

4. Pierce SM, Recht A, Lingos TI, Abner A, Vicini F, Silver B, Herzog A, Harris JR, Long-term radiation complications following conservative surgery (CS) and radiation therapy (RT) in patients with early stage breast cancer. Int J Radiat Oncol Biol Phys 23, 915–923 (1992). [PubMed: 1639653]

5. Baxter NN, Habermann EB, Tepper JE, Durham SB, Virnig BA, Risk of pelvic fractures in older women following pelvic irradiation. JAMA 294, 2587–2593 (2005). [PubMed: 16304072]

6. Park SH, Kim JC, Lee JE, Park IK, Pelvic insufficiency fracture after radiotherapy in patients with cervical cancer in the era of PET/CT. Radiat Oncol J 29, 269–276 (2011). [PubMed: 22984680]

7. Kwon JW, Huh SJ, Yoon YC, Choi SH, Jung JY, Oh D, Choe BK, Pelvic bone complications after radiation therapy of uterine cervical cancer: evaluation with MRI. AJR Am J Roentgenol 191, 987–994 (2008). [PubMed: 18806132]

8. Uezono H, Tsujino K, Moriki K, Nagano F, Ota Y, Sasaki R, Soejima T, Pelvic insufficiency fracture after definitive radiotherapy for uterine cervical cancer: retrospective analysis of risk factors. J Radiat Res 54, 1102–1109 (2013). [PubMed: 23685668]

9. Holt GE, Griffin AM, Pintilie M, Wunder JS, Catton C, O'Sullivan B, Bell RS, Fractures following radiotherapy and limb-salvage surgery for lower extremity soft-tissue sarcomas. A comparison of high-dose and low-dose radiotherapy. J Bone Joint Surg Am 87, 315–319 (2005). [PubMed: 15687153]

10. Siegel RL, Miller KD, Fuchs HE, Jemal A, Cancer Statistics, 2021. CA Cancer J Clin 71, 7–33 (2021). [PubMed: 33433946]

11. Cao X, Wu X, Frassica D, Yu B, Pang L, Xian L, Wan M, Lei W, Armour M, Tryggestad E, Wong J, Wen CY, Lu WW, Frassica FJ, Irradiation induces bone injury by damaging bone marrow microenvironment for stem cells. Proc Natl Acad Sci U S A 108, 1609–1614 (2011). [PubMed: 21220327]

12. Chen Q, Liu Y, Jeong HW, Stehling M, Dinh VV, Zhou B, Adams RH, Apelin(+) Endothelial Niche Cells Control Hematopoiesis and Mediate Vascular Regeneration after Myeloablative Injury. Cell Stem Cell 25, 768–783 e766 (2019). [PubMed: 31761723]

13. Bai J, Wang Y, Wang J, Zhai J, He F, Zhu G, Irradiation-induced senescence of bone marrow mesenchymal stem cells aggravates osteogenic differentiation dysfunction via paracrine signaling. Am J Physiol Cell Physiol 318, C1005–C1017 (2020). [PubMed: 32233952]

14. Zhong L, Yao L, Holdreith N, Yu W, Gui T, Miao Z, Elkaim Y, Li M, Gong Y, Pacifici M, Maity A, Busch TM, Joeng KS, Cengel K, Seale P, Tong W, Qin L, Transient expansion and myofibroblast conversion of adipogenic lineage precursors mediate bone marrow repair after radiation. JCI Insight 7, (2022).

15. Spencer JA, Ferraro F, Roussakis E, Klein A, Wu J, Runnels JM, Zaher W, Mortensen LJ, Alt C, Turcotte R, Yusuf R, Cote D, Vinogradov SA, Scadden DT, Lin CP, Direct measurement of local oxygen concentration in the bone marrow of live animals. Nature 508, 269–273 (2014). [PubMed: 24590072]

16. Wan C, Gilbert SR, Wang Y, Cao X, Shen X, Ramaswamy G, Jacobsen KA, Alaql ZS, Eberhardt AW, Gerstenfeld LC, Einhorn TA, Deng L, Clemens TL, Activation of the hypoxia-inducible factor-1alpha pathway accelerates bone regeneration. Proc Natl Acad Sci U S A 105, 686–691 (2008). [PubMed: 18184809]

17. Shomento SH, Wan C, Cao X, Faugere MC, Bouxsein ML, Clemens TL, Riddle RC, Hypoxia-inducible factors 1alpha and 2alpha exert both distinct and overlapping functions in long bone development. J Cell Biochem 109, 196–204 (2010). [PubMed: 19899108]

18. Araldi E, Khatri R, Giaccia AJ, Simon MC, Schipani E, Lack of HIF-2alpha in limb bud mesenchyme causes a modest and transient delay of endochondral bone development. Nat Med 17, 25–26; author reply 27-29 (2011). [PubMed: 21217667]
19. Kusumbe AP, Ramasamy SK, Itkin T, Mae MA, Langen UH, Betsholtz C, Lapidot T, Adams RH, Age-dependent modulation of vascular niches for haematopoietic stem cells. Nature 532, 380–384 (2016). [PubMed: 27074508]
20. Kusumbe AP, Ramasamy SK, Adams RH, Coupling of angiogenesis and osteogenesis by a specific vessel subtype in bone. Nature 507, 323 (2014). [PubMed: 24646994]
21. Takubo K, Goda N, Yamada W, Iriuchishima H, Ikeda E, Kubota Y, Shima H, Johnson RS, Hirao A, Suematsu M, Suda T, Regulation of the HIF-1alpha level is essential for hematopoietic stem cells. Cell Stem Cell 7, 391–402 (2010). [PubMed: 20804974]
22. Mendez-Ferrer S, Michurina TV, Ferraro F, Mazloom AR, Macarthur BD, Lira SA, Scadden DT, Ma'ayan A, Enikolopov GN, Frenette PS, Mesenchymal and haematopoietic stem cells form a unique bone marrow niche. Nature 466, 829–834 (2010). [PubMed: 20703299]
23. Zhou BO, Yue R, Murphy MM, Peyer JG, Morrison SJ, Leptin-receptor-expressing mesenchymal stromal cells represent the main source of bone formed by adult bone marrow. Cell Stem Cell 15, 154–168 (2014). [PubMed: 24953181]
24. Greenbaum A, Hsu YM, Day RB, Schuettpelz LG, Christopher MJ, Borgerding JN, Nagasawa T, Link DC, CXCL12 in early mesenchymal progenitors is required for haematopoietic stem-cell maintenance. Nature 495, 227–230 (2013). [PubMed: 23434756]
25. Ono N, Ono W, Nagasawa T, Kronenberg HM, A subset of chondrogenic cells provides early mesenchymal progenitors in growing bones. Nat Cell Biol 16, 1157–1167 (2014). [PubMed: 25419849]
26. Lee SY, Park KH, Yu HG, Kook E, Song WH, Lee G, Koh JT, Shin HI, Choi JY, Huh YH, Ryu JH, Controlling hypoxia-inducible factor-2alpha is critical for maintaining bone homeostasis in mice. Bone Res 7, 14 (2019). [PubMed: 31098335]
27. Merceron C, Ranganathan K, Wang E, Tata Z, Makkapati S, Khan MP, Mangiavini L, Yao AQ, Castellini L, Levi B, Giaccia AJ, Schipani E, Hypoxia-inducible factor 2alpha is a negative regulator of osteoblastogenesis and bone mass accrual. Bone Res 7, 7 (2019). [PubMed: 30792937]
28. Jonasch E, Donskov F, Iliopoulos O, Rathmell WK, Narayan VK, Maughan BL, Oudard S, Else T, Maranchie JK, Welsh SJ, Thamake S, Park EK, Perini RF, Linehan WM, Srinivasan R, Investigators MK, Belzutifan for Renal Cell Carcinoma in von Hippel-Lindau Disease. N Engl J Med 385, 2036–2046 (2021). [PubMed: 34818478]
29. Choueiri TK, Bauer TM, Papadopoulos KP, Plimack ER, Merchan JR, McDermott DF, Michaelson MD, Appleman LJ, Thamake S, Perini RF, Zojwalla NJ, Jonasch E, Inhibition of hypoxia-inducible factor-2alpha in renal cell carcinoma with belzutifan: a phase 1 trial and biomarker analysis. Nat Med 27, 802–805 (2021). [PubMed: 33888901]
30. Hoque J, Shih YV, Zeng Y, Newman H, Sangaj N, Arjunji N, Varghese S, Bone targeting nanocarrier-assisted delivery of adenosine to combat osteoporotic bone loss. Biomaterials 273, 120819 (2021). [PubMed: 33892345]
31. Zeng Y, Hoque J, Varghese S, Biomaterial-assisted local and systemic delivery of bioactive agents for bone repair. Acta Biomater 93, 152–168 (2019). [PubMed: 30711659]
32. Stapleton M, Sawamoto K, Almeciga-Diaz CJ, Mackenzie WG, Mason RW, Orii T, Tomatsu S, Development of Bone Targeting Drugs. Int J Mol Sci 18, (2017). [PubMed: 29267212]
33. Downes NL, Laham-Karam N, Kaikkonen MU, Yla-Herttuala S, Differential but Complementary HIF1alpha and HIF2alpha Transcriptional Regulation. Mol Ther 26, 1735–1745 (2018). [PubMed: 29843956]
34. Tencerova M, Figeac F, Ditzel N, Taipaleenmaki H, Nielsen TK, Kassem M, High-Fat Diet-Induced Obesity Promotes Expansion of Bone Marrow Adipose Tissue and Impairs Skeletal Stem Cell Functions in Mice. J Bone Miner Res 33, 1154–1165 (2018). [PubMed: 29444341]
35. Cho H, Du X, Rizzi JP, Liberzon E, Chakraborty AA, Gao W, Carvo I, Signoretti S, Bruick RK, Josey JA, Wallace EM, Kaelin WG, On-target efficacy of a HIF-2alpha antagonist in preclinical kidney cancer models. Nature 539, 107–111 (2016). [PubMed: 27595393]

36. Chen SY, Yu HT, Kao JP, Yang CC, Chiang SS, Mishchuk DO, Mau JL, Slupsky CM, An NMR metabolomic study on the effect of alendronate in ovariectomized mice. PLoS One 9, e106559 (2014). [PubMed: 25184758]
37. Corral DA, Amling M, Priemel M, Loyer E, Fuchs S, Ducy P, Baron R, Karsenty G, Dissociation between bone resorption and bone formation in osteopenic transgenic mice. Proc Natl Acad Sci U S A 95, 13835–13840 (1998). [PubMed: 9811887]
38. Liu W, Toyosawa S, Furuichi T, Kanatani N, Yoshida C, Liu Y, Himeno M, Narai S, Yamaguchi A, Komori T, Overexpression of Cbfa1 in osteoblasts inhibits osteoblast maturation and causes osteopenia with multiple fractures. J Cell Biol 155, 157–166 (2001). [PubMed: 11581292]
39. Martin JF, Olson EN, Identification of a prx1 limb enhancer. Genesis 26, 225–229 (2000). [PubMed: 10748458]
40. Shu HS, Liu YL, Tang XT, Zhang XS, Zhou B, Zou W, Zhou BO, Tracing the skeletal progenitor transition during postnatal bone formation. Cell Stem Cell 28, 2122–2136 e2123 (2021). [PubMed: 34499868]
41. Ortinau LC, Wang H, Lei K, Deveza L, Jeong Y, Hara Y, Grafe I, Rosenfeld SB, Lee D, Lee B, Scadden DT, Park D, Identification of Functionally Distinct Mx1+alphaSMA+ Periosteal Skeletal Stem Cells. Cell Stem Cell 25, 784–796 e785 (2019). [PubMed: 31809737]
42. Matsushita Y, Nagata M, Kozloff KM, Welch JD, Mizuhashi K, Tokavanich N, Hallett SA, Link DC, Nagasawa T, Ono W, Ono N, A Wnt-mediated transformation of the bone marrow stromal cell identity orchestrates skeletal regeneration. Nat Commun 11, 332 (2020). [PubMed: 31949165]
43. Zhou BO, Yu H, Yue R, Zhao Z, Rios JJ, Naveiras O, Morrison SJ, Bone marrow adipocytes promote the regeneration of stem cells and haematopoiesis by secreting SCF. Nat Cell Biol 19, 891–903 (2017). [PubMed: 28714970]
44. Kim J, Jung Y, Sun H, Joseph J, Mishra A, Shiozawa Y, Wang J, Krebsbach PH, Taichman RS, Erythropoietin mediated bone formation is regulated by mTOR signaling. J Cell Biochem 113, 220–228 (2012). [PubMed: 21898543]
45. Hiram-Bab S, Liron T, Deshet-Unger N, Mittelman M, Gassmann M, Rauner M, Franke K, Wielockx B, Neumann D, Gabet Y, Erythropoietin directly stimulates osteoclast precursors and induces bone loss. FASEB J 29, 1890–1900 (2015). [PubMed: 25630969]
46. Mo C, Guo J, Qin J, Zhang X, Sun Y, Wei H, Cao D, Zhang Y, Zhao C, Xiong Y, Zhang Y, Sun Y, Shen L, Yue R, Single-cell transcriptomics of LepR-positive skeletal cells reveals heterogeneous stress-dependent stem and progenitor pools. EMBO J, e108415 (2021). [PubMed: 34957577]
47. Tikhonova AN, Dolgalev I, Hu H, Sivaraj KK, Hoxha E, Cuesta-Dominguez A, Pinho S, Akhmetzyanova I, Gao J, Witkowski M, Guillamot M, Gutkin MC, Zhang Y, Marier C, Diefenbach C, Kousteni S, Heguy A, Zhong H, Fooksman DR, Butler JM, Economides A, Frenette PS, Adams RH, Satija R, Tsirigos A, Aifantis I, The bone marrow microenvironment at single-cell resolution. Nature 569, 222–228 (2019). [PubMed: 30971824]
48. Damek-Poprawa M, Stefanik D, Levin LM, Akintoye SO, Human bone marrow stromal cells display variable anatomic site-dependent response and recovery from irradiation. Arch Oral Biol 55, 358–364 (2010). [PubMed: 20378097]
49. Prasad SR, Kumar TSS, Jayakrishnan A, Nanocarrier-based drug delivery systems for bone cancer therapy: a review. Biomed Mater 16, (2021).
50. Yaprak G, Gemici C, Temizkan S, Ozdemir S, Dogan BC, Seseogullari OO, Osteoporosis development and vertebral fractures after abdominal irradiation in patients with gastric cancer. BMC Cancer 18, 972 (2018). [PubMed: 30309324]
51. Rankin EB, Wu C, Khatri R, Wilson TL, Andersen R, Araldi E, Rankin AL, Yuan J, Kuo CJ, Schipani E, Giaccia AJ, The HIF signaling pathway in osteoblasts directly modulates erythropoiesis through the production of EPO. Cell 149, 63–74 (2012). [PubMed: 22464323]
52. Parfitt AM, Drezner MK, Glorieux FH, Kanis JA, Malluche H, Meunier PJ, Ott SM, Recker RR, Bone histomorphometry: standardization of nomenclature, symbols, and units. Report of the ASBMR Histomorphometry Nomenclature Committee. J Bone Miner Res 2, 595–610 (1987). [PubMed: 3455637]

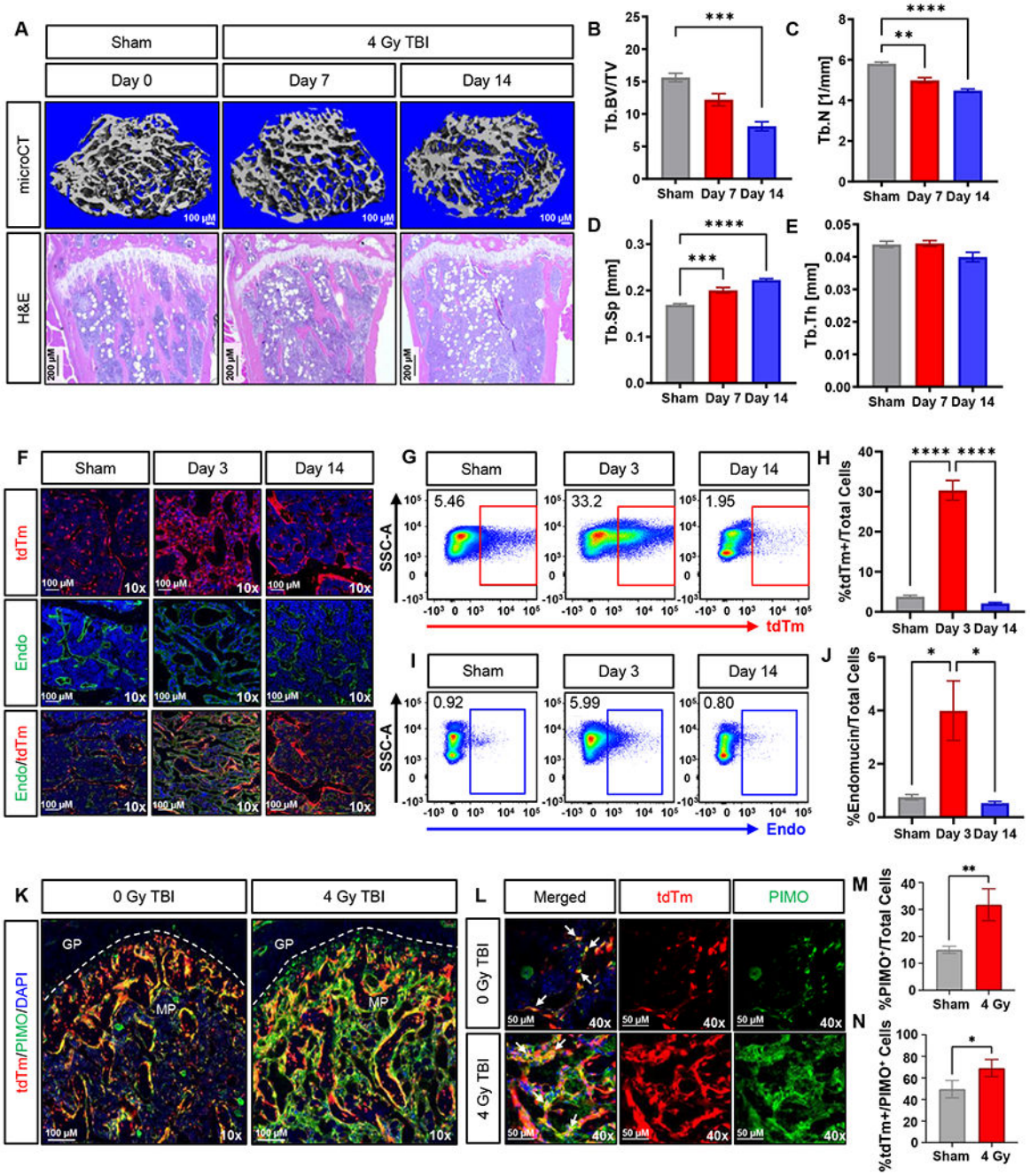

Fig. 1. Radiation exposure disrupts the hypoxic bone microenvironment and is associated with a transient expansion of LepR+ stromal cells.

(**A**) Representative microCT and hematoxylin and eosin (H&E) images from 12-16 week old wild type (WT) mice that were untreated (sham 0 Gy) ($n = 17$) or treated with 4 Gy total body irradiation (TBI) ($n = 3$); scale bar 200 μm. (**B to E**) MicroCT analyses of trabecular bone parameters, (sham, $n = 17$; irradiated, $n = 3$). (**B**) Trabecular bone volume/tissue volume (Tb.BV/TV), (**C**) trabecular number (Tb.N, 1/mm), (**D**) trabecular separation (Tb.Sp, mm), and (**E**) trabecular thickness (Tb.Th, mm) values are shown. (**F**) Fluorescent images of

Lepr-tdTm mouse femoral bone. tdTomato+ cells (tdTm, red) and endomucin+ cells (endo, green), 3 and 14 days post-irradiation (4 Gy TBI). (**G**) Representative flow cytometry plots and (**H**) quantification of percent tdTm+ cells. (**I**) Representative flow cytometry plots and (**J**) quantification of percent endo+ cells from bone marrow aspirates of *Lepr*-tdTm animals at 3 and 14 days post-irradiation (4 Gy TBI); (sham, $n = 5$; irradiated day 3, $n = 4$; irradiated day 14, $n = 7$). SSC-A, side scatter area. (**K and L**) Fluorescent pimonidazole (PIMO) staining (green) in femoral bone of *Lepr*-tdTm mice 3 days post-irradiation (4 Gy TBI). Growth plate (GP), metaphysis (MP), pimonidazole and *Lepr*-tdTm+ cells (white arrows) ($n = 3$). (**M**) Percentage of PIMO+ cells per total cells and (**N**) percent tdTm+ cells per PIMO+ cells 3 days post-irradiation (4 Gy TBI). Scale bars: 10x: 100 μm, 40x: 50 μm. ($n = 3$). Data are presented as means ± SEM. Statistical analysis was performed using either (**M and N**) Student's t-test or (**B, C, D, E, H, and J**) one-way ANOVA with Tukey's post hoc test. *$p < 0.05$, **$p < 0.01$, ***$p < 0.001$, and ****$p < 0.0001$.

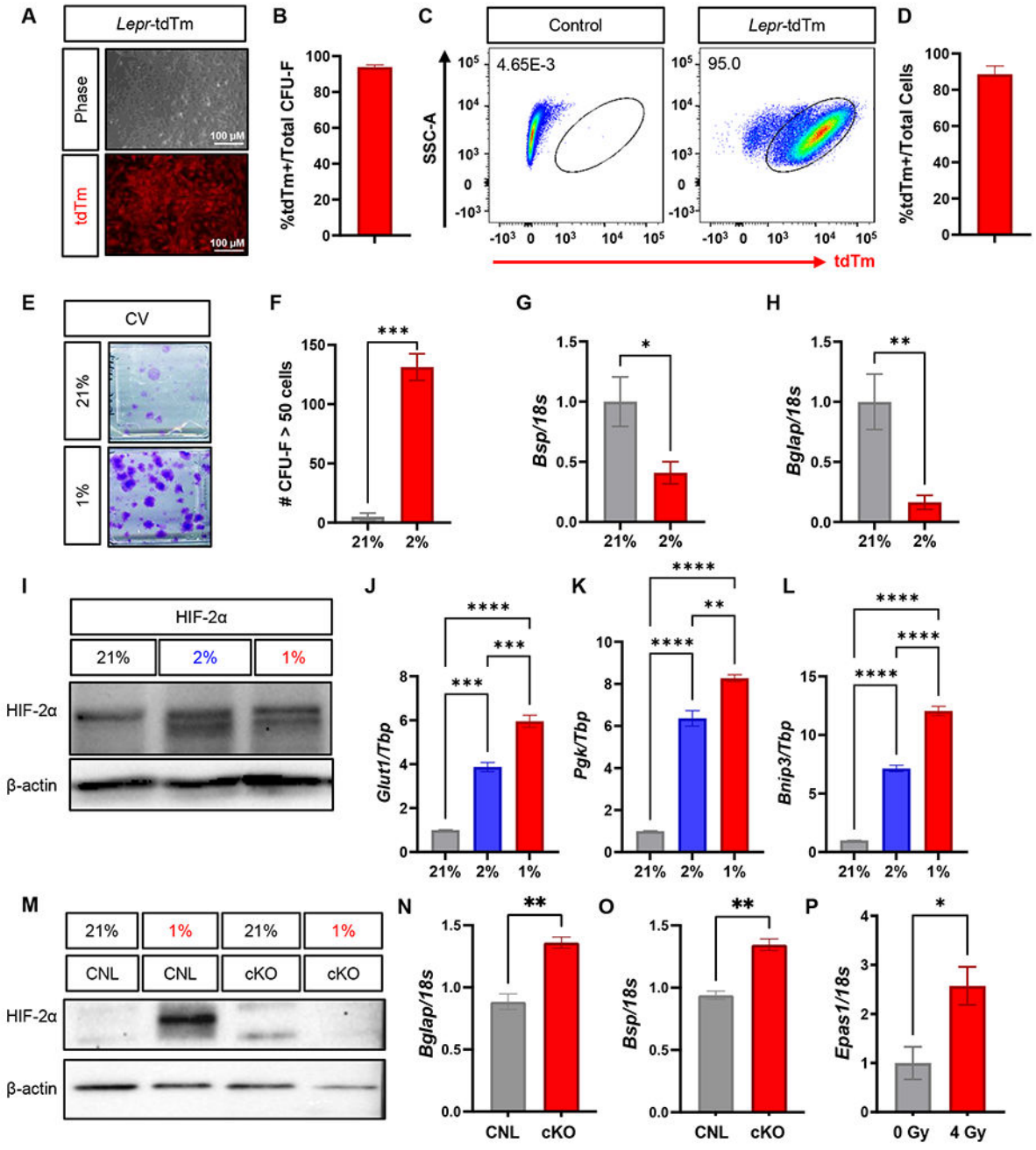

Fig. 2. BMSCs and LepR+ cells respond to hypoxia by decreasing mineralization and stabilizing HIF-2α.

(**A**) Representative phase and fluorescent images of a tdTm+ colony and (**B**) quantification of percent of tdTm+ colonies per total colonies isolated from *Lepr*-tdTm mice ($n = 4$). (**C**) Representative flow cytometry scatter plots and (**D**) quantification of tdTm+ cells per total number of cells in BMSCs isolated from control and *Lepr*-tdTm animals ($n = 3$). (**E**) Representative images and (**F**) quantification of crystal violet (CV) stained colony-forming unit-fibroblast (CFU-F) assays from BMSCs isolated from WT control mice under

normoxic 21% O_2 and hypoxic 1% O_2 conditions ($n = 3$). (**G and H**) Quantitative reverse transcription-PCR (qRT-PCR) of osteogenic BMSC cultures incubated in 21% O_2 and 1% O_2 for (**G**) *Bsp* and (**H**) *Bglap* ($n = 3$). (**I**) Representative western blot of HIF-2α protein in BMSCs under 21%, 2%, or 1% O_2 conditions. (**J to L**) qRT-PCR of BMSC cultures incubated under 21%, 2% or 1% O_2 conditions measuring mRNA expression of HIF target genes including (**J**) *Glut1*, (**K**) *Pgk*, and (**L**) *Bnip3.* ($n = 3$). (**M**) Representative western blot analysis of HIF-2α from BMSCs isolated from $Epas^{fl/fl}$ control (CNL) and HIF-2α cKO knockout mice (cKO) under 21% O_2 and 1% O_2 conditions ($n = 2$). (**N and O**) qRT-PCR of osteogenic BMSC cultures isolated from control and HIF-2α cKO for (**N**) *Bglap* and (**O**) *Bsp* ($n = 3$). (**P**) qRT-PCR of *Epas1* from whole bone homogenates isolated from non-irradiated and 4 Gy TBI animals ($n = 3$). Scale bar 100 μm. Statistical analysis was performed using (**F, G, H, N, O, and P**) Student's t-test or (**J, K, and L**) one-way ANOVA with Tukey's post hoc test as appropriate. Data are presented as means ± SEM. $*p < 0.05$, $**p < 0.01$, $***p < 0.001$, and $****p < 0.0001$.

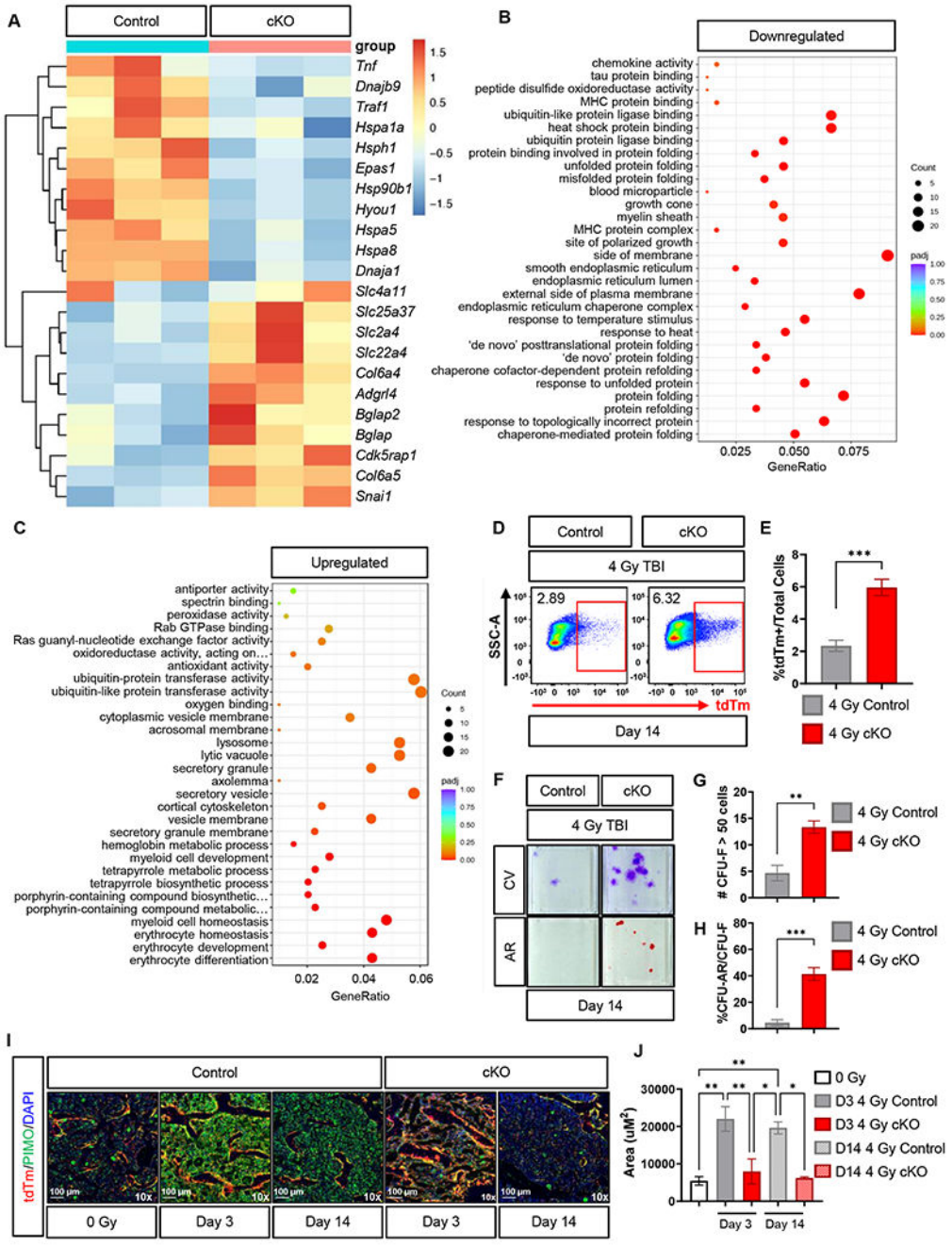

Fig. 3. HIF-2α cKO alters the transcriptome of LepR+ cells and maintains a homeostatic hypoxic microenvironment following radiation injury.

(**A**) Transcriptomic analysis displayed as a heatmap showing a portion of differentially expressed genes (DEG) center-scaled by row (≥ 1.5 expression change, $p < 0.05$). (**B and C**) GO functional enrichment analysis of DEGs highlighting (**B**) downregulated and (**C**) upregulated putative processes when comparing $tdTm^+$ cells isolated from irradiated *Lepr*-tdTm control to irradiated *Lepr*-tdTm-HIF-2α cKO animals; all cells were collected 14 days post-irradiation ($n = 3$ per group). FDR ≥ 0.05. (**D**) Representative flow cytometry

plots and (**E**) analysis of percentage of tdTm+ cells from bone marrow aspirates of irradiated *Lepr*-tdTm (control, $n = 7$) and *Lepr*-tdTm-HIF-2α cKO ($n = 3$) animals at 14 days post-irradiation. (**F**) Representative images and quantification of CFU-F assays from irradiated *Epas-1*$^{fl/fl}$ control and HIF-2α cKO mice stained with (**G**) crystal violet (CV) and (**H**) alizarin red (AR), ($n = 3$ per group). (**I**) Representative fluorescent images and (**J**) quantification of images of femoral bones isolated from *Lepr*-tdTm control and *Lepr*-tdTm-HIF-2α cKO mice, stained with pimonidazole staining (PIMO, green) 3 days following 4 Gy TBI ($n = 3$). Scale bar 10x - 100 μm. Statistical analysis was performed using (**E, G and H**) Student's t-test or (**J**) one-way ANOVA with Tukey's post hoc test. Data are presented as means ± SEM. *$p < 0.05$, **$p < 0.01$, and ***$p < 0.001$.

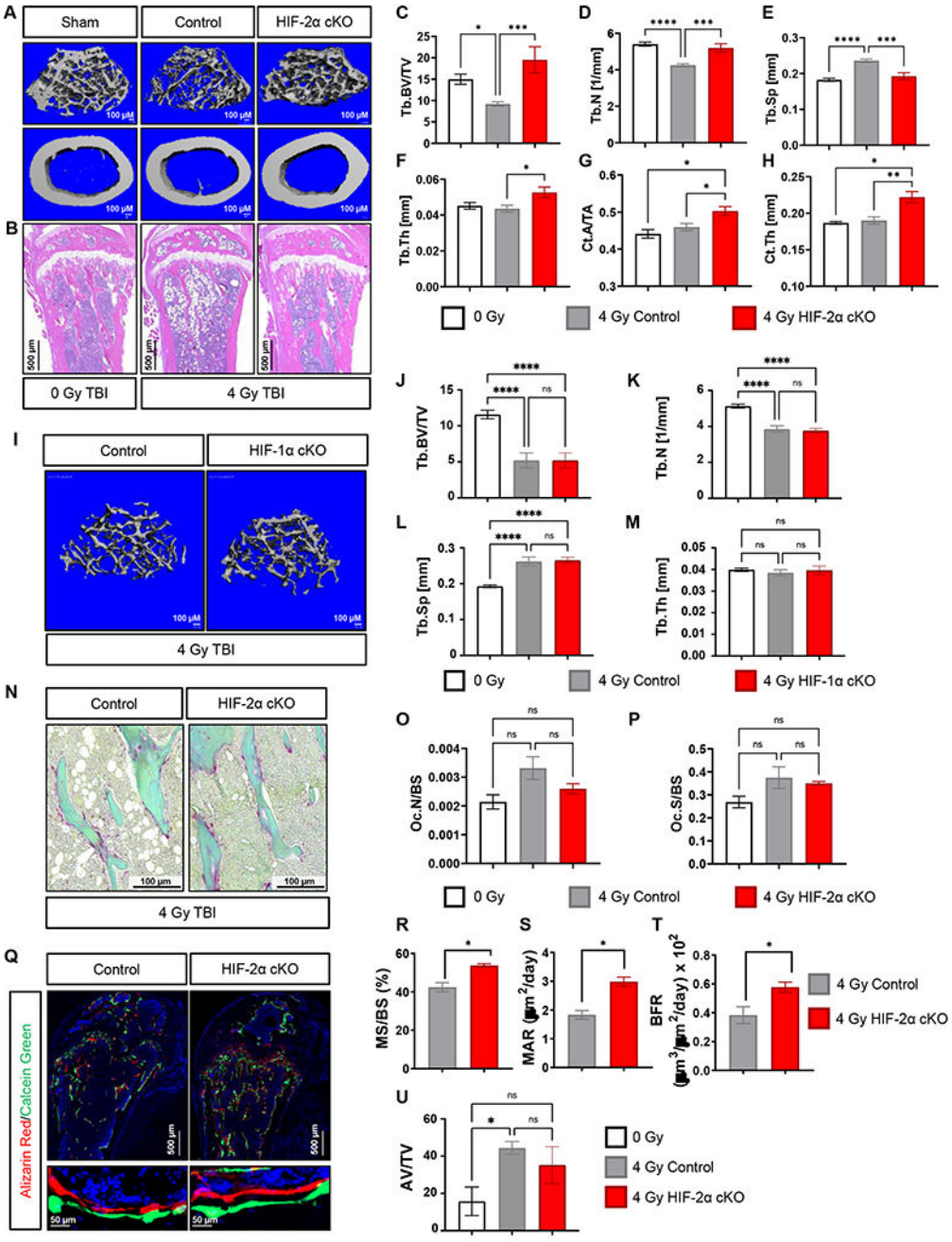

Fig. 4. HIF-2α deletion in *Lepr*-expressing cells prevents radiation-induced bone loss and promotes downstream osteoblast activity.

(**A**) Representative microCT of trabecular bone (upper panel), and cortical bone (lower panel). (**B**) H&E histological images from 12-16 week old non-irradiated and irradiated control and HIF-2α cKO animals. Scale bar 200 μm. (**C to H**) MicroCT analyses of bone parameters: (**C**) Tb.BV/TV, (**D**) Tb.N (1/mm), (**E**) Tb.Sp (mm), (**F**) Tb.Th (mm). (**G**) cortical area/tissue area (Ct.A/TA), and (**H**) cortical thickness (Ct.Th) (mm). non-irradiated (n = 6) and irradiated control (n = 7) and HIF-2α cKO animals (n = 4). (**I**) Representative

microCT images from 12-16 week old *Hif-1a*$^{fl/fl}$ (control) and *Lepr*-specific HIF-1α cKO (HIF-1α cKO) animals. (**J to M**) MicroCT analyses of trabecular bone parameters of control animals treated with 0 Gy ($n = 10$) or 4Gy control ($n = 5$), as well as HIF-1α cKO animals treated with 4Gy ($n = 5$). (**J**) Tb.BV/TV, (**K**) Tb.N (1/mm), (**L**) Tb.Sp, (mm), and (**M**) Tb.Th (mm) are shown. (**N**) Representative TRAP-stained tissue sections ($n = 3$) and quantification of (**O**) osteoclast number/bone surface (Oc.N/BS) ($n = 3$) and (**P**) osteoclast surface/bone surface (Oc.S/BS) ($n = 3$). Scale bar 100 μm. (**Q**) Representative calcein (green) and alizarin red (red) double labeled sections of the distal femur. Scale bar 500 μm (upper panel) and 50μm (lower panel). (**R to T**) Analysis of dynamic histomorphometric parameters including (**R**) mineralizing surface/bone (MS/BS) (%) surface, (**S**) mineral apposition rate (MAR) (μm^2/day), and (**T**) bone formation rate (BFR) ($\mu m^3/\mu m^2$/day). ($n = 3$) . (**U**) Quantification of osmium tetroxide staining presented as adipose volume/total volume (AV/TV); 0 Gy Control ($n = 4$), 4 Gy Control ($n = 7$), 4 Gy HIF-2α cKO ($n = 4$). All analysis were performed on mice 14 days post-4 Gy TBI. Statistical analysis was performed using (**R, S, and T**) Student's t-test or one-way (**C, D, E, F, G, H, J, K, L, M, O, P, and U**) ANOVA with Tukey's post hoc test as appropriate. Data are presented as means ± SEM. $*p < 0.05$, $**p < 0.01$, and $***p < 0.001$.

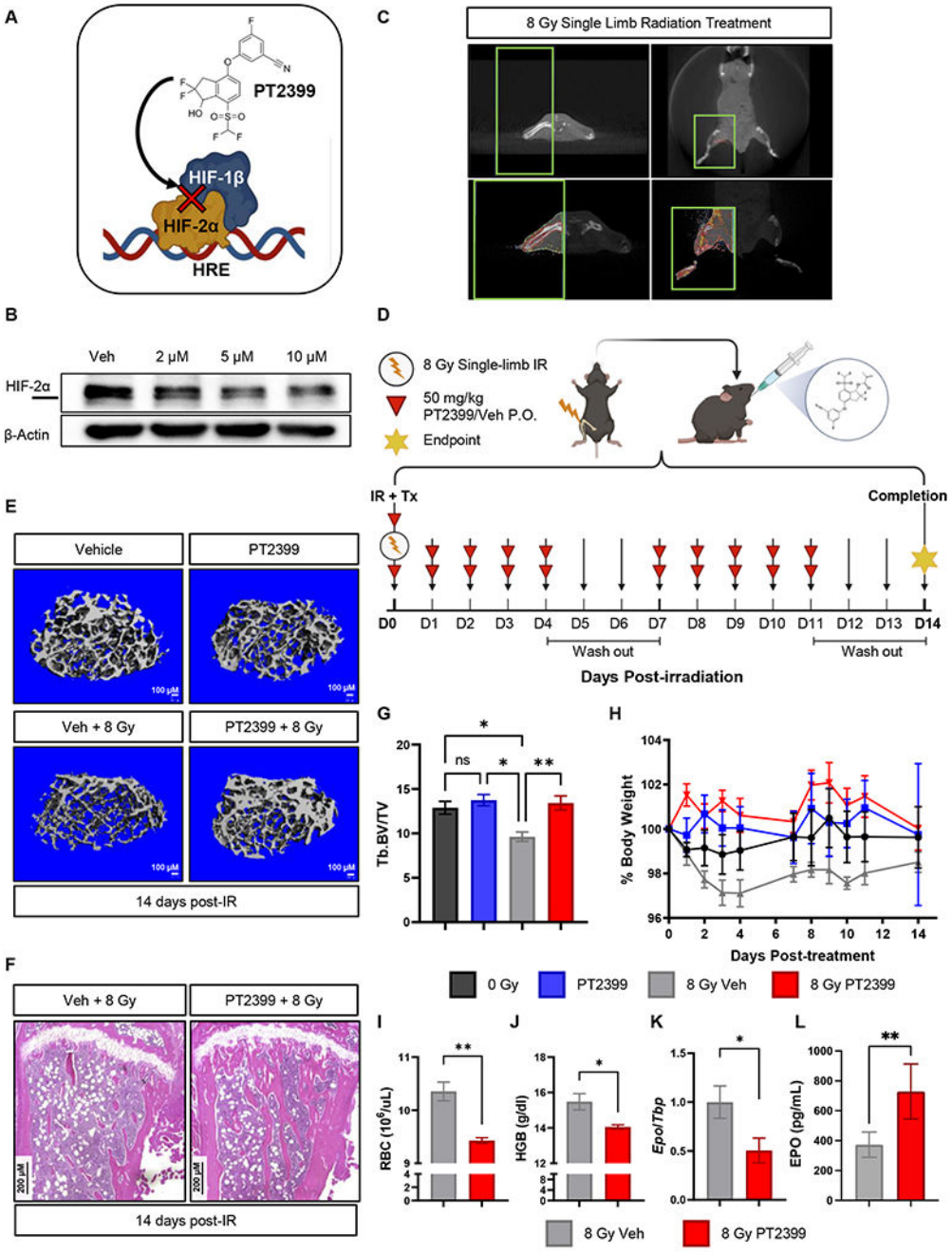

Fig. 5. Oral PT2399 treatment ameliorates bone loss and induces mildly anemic phenotype following 8 Gy single limb radiation.

(**A**) Schematic of PT2399-mediated inhibition of HIF-2α. (**B**) Western blot analysis of HIF-2α in BMSCs treated with PT2399 ($n = 2$). (**C**) Schematic of single limb radiation treatment protocol. Green boxes showing the region of right hindlimb receiving 100% of 8 Gy, anterior-posterior/posterior-anterior (AP/PA) beams. (**D**) Schematic of oral PT2399 treatment regimen. (**E**) Representative microCT and (**F**) histological images of 12 week old non-irradiated and irradiated WT mice treated with vehicle or oral PT2399. Scale bar 200

μm (**G**) microCT analyses of Tb.BV/TV from non-irradiated mice treated with vehicle (n = 10) or PT2399 (n = 4) and irradiated WT mice treated with vehicle (n = 8) or PT2399 (n = 9). (**H**) Percentage body weight of animals across experimental time course. (**I**) Red blood cell (RBC) counts and (**J**) hemoglobin (HGB) of irradiated vehicle and PT2399 treated animals analyzed from whole blood CBC analysis. $n \geq 4$ per group. (**K**) qRT-PCR analyses of *Epo* from kidney homogenates of irradiated vehicle and PT2399 treated animals, Tata box binding protein (*Tbp)* was used as a housekeeping gene. (**L**) Analysis of EPO in serum determined by ELISA in vehicle or PT2399 treated mice (n = 5). All analysis were performed on mice 14 days post-irradiation. Statistical analysis was performed using (**I, J, K, and L**) Student's t-test or (**G and H**) one-way ANOVA with Tukey's post hoc test as appropriate. Data are presented as means ± SEM. *$p < 0.05$, **$p < 0.01$, and ***$p < 0.001$.

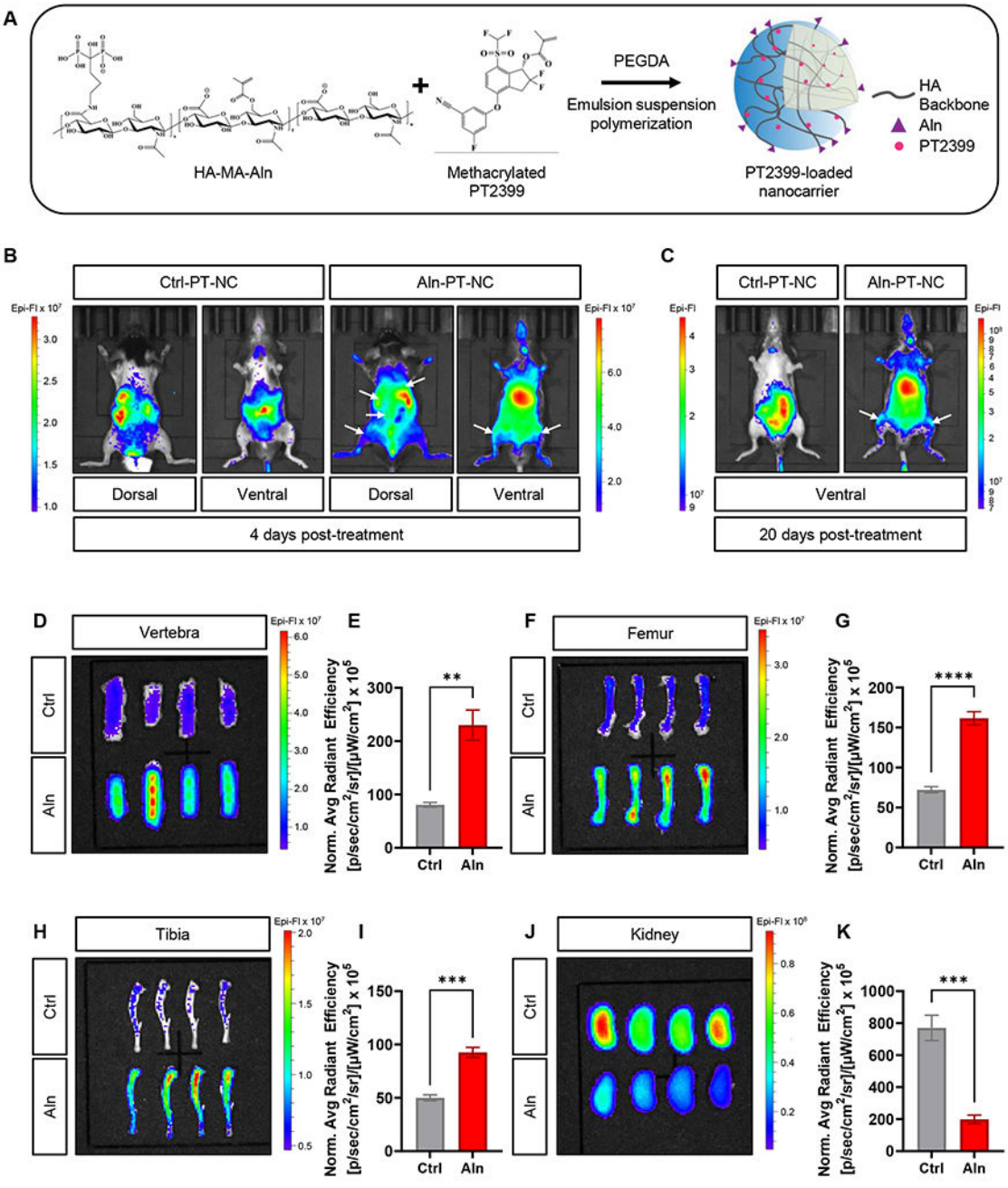

Fig. 6. Aln-PT-NC exhibit increased targeting to bone tissue and reduced accumulation in the kidney.

(**A**) Abbreviated schematic of Aln-PT-NC synthesis and drug loading. (**B**) In vivo fluorescence images of fluorescently-labeled non-targeted PT2399-loaded (Ctrl-PT-NC) and Alendronate (Aln)-conjugated PT2399 loaded (Aln-PT-NC) nanocarrier distribution 4 days and (**C**) 20 days post-treatment. ($n = 3$). Nanocarriers were conjugated with similar amounts of Cy7 dye for visualization by IVIS imaging. White arrows indicate Cy7-conjugated Aln-PT-NC colocalized to bone. (**D**) Representative IVIS images and (**E**) quantification

of average radiant efficiency represented per gram of the tissue of non-targeted (Ctrl) and bone-targeted (Aln) nanocarrier in the vertebra, (**F and G**) femur, (**H and I**) tibia, and (**J and K**) kidney. $n = 4$ per group. Statistical analysis was performed using Student's t-test. Data are presented as means ± SEM. *$p < 0.05$, **$p < 0.01$, ***$p < 0.001$, and ****$p < 0.0001$.

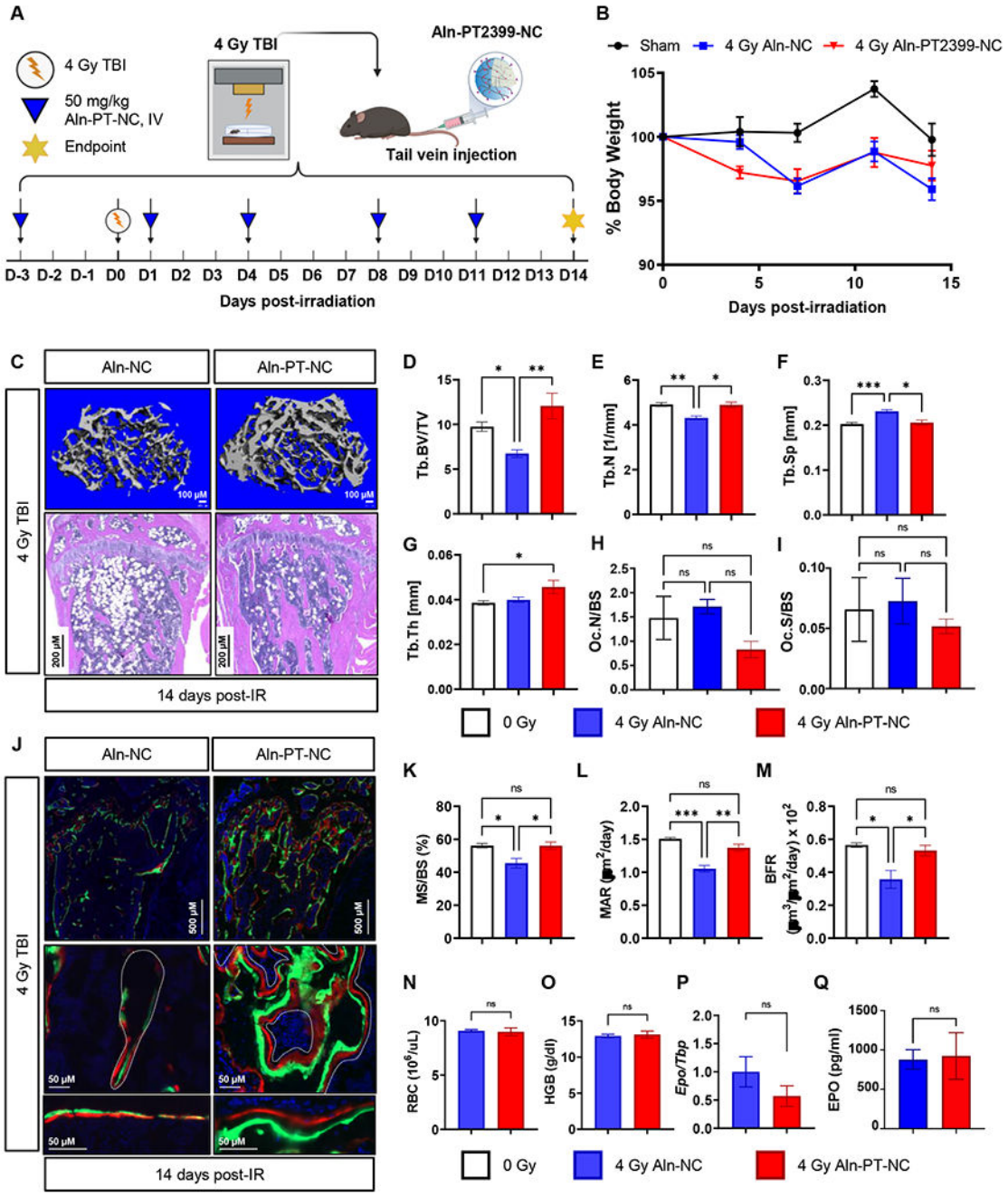

Fig. 7. Aln-PT-NC treatment protects against bone loss associated with 4 Gy total body irradiation and attenuates anemic phenotype.

(**A**) Schematic of nanocarrier treatment regimen. (**B**) Percentage body weight of experimental animals across 14 days of treatment with unloaded Aln-conjugated nanocarrier (Aln-NC) and PT2399-loaded Aln-conjugated nanocarrier (Aln-PT-NC). (**C**) MicroCT and H&E images of Aln-NC and Aln-PT-NC treated animals (n = 5 per group). Scale bar 200 μm. (**D to G**) Quantification of trabecular bone parameters of Aln-NC and Aln-PT-NC treated animals at 14 days post-irradiation (n = 5 per group). Shown are (**D**) Tb.BV/TV,

(**E**) Tb.N (1/mm), (**F**) Tb.N (mm), and (**G**) Tb.Sp (mm). Quantification of (**H**) Oc.N/BS and (**I**) Oc.S/BS. (**J**) Representative calcein (green) and alizarin red (red) double labeled sections of the distal femur from irradiated Aln-NC and Aln-PT-NC treated mice ($n = 4$) Scale bar 500 μm (upper panel) and 50μm (middle and lower panels). (**K to M**) Analysis of dynamic histomorphometric parameters using double labeling, reporting (**K**) MS/BS (%) (**L**) MAR (μm^2/day), and (**M**) BFR ($\mu m^3/\mu m^2$/day) n = 3 per group. (**N**) RBC counts and (**O**) HGB analyzed from whole blood CBC analysis. (**P**) RT-qPCR analyses of *Epo* from kidney homogenates of Aln-NC and Aln-PT-NC treated mice. (**Q**) Analysis of EPO in serum determined by ELISA in Aln-NC and Aln-PT-NC treated mice. All analysis were performed on mice 14 days post-irradiation, $n \geq 5$ per group, unless otherwise noted. Statistical analysis was performed using (**N, O, P, and Q**) Student's t-test or (**B, D, E, F, G, H, I, K, L, and M**) one-way ANOVA with Tukey's post hoc test as appropriate. Data are presented as means ± SEM. *$p < 0.05$, **$p < 0.01$, and ***$p < 0.001$.